Supporting Information

Deactivation Pathway of Ras GTPase Underlies Conformational Substates as Targets for Drug Design

Shaoyong Lu[*,†,§], Duan Ni[†,§], Chengxiang Wang[†,§], Xinheng He[†], Houwen Lin[‡], Zheng Wang,[*,±] and Jian Zhang[*,†]

[†]Key Laboratory of Cell Differentiation and Apoptosis of Chinese Ministry of Education, Clinical and Fundamental Research Center, Department of Pharmacy, Renji Hospital, Shanghai Jiao Tong University, School of Medicine, Shanghai 200127, China

[‡]Research Center for Marine Drugs, State Key Laboratory of Oncogenes and Related Genes, Department of Pharmacy, Renji Hospital, Shanghai Jiao Tong University, School of Medicine, Shanghai, 200127, China

[±]Department of Gastrointestinal Surgery, Renji Hospital, Shanghai Jiao Tong University, School of Medicine, Shanghai 200127, China

[§]S.L., D.N., and C.W. contributed equally to this work.

*To whom correspondence should be addressed:

Dr. Jian Zhang, E-mail: jian.zhang@sjtu.edu.cn

Dr. Zheng Wang, E-mail: wangzh1972@126.com

Dr. Shaoyong Lu, E-mail: lushaoyong@yeah.net

Section 1: Details of Nudged Elastic Band (NEB) Method and Molecular Dynamics (MD) Simulations

1.1 Simulation Systems Setup

The GTP-analog, GppNHp-bound K-Ras^{Q61H} (PDB ID: 3GFT) and GDP-bound K-Ras (PDB ID: 4LPK)[1] were extracted from the Protein Data Bank (PDB) as the two end-point structures, the former active form as the starting structure and the latter inactive form as the ending structure. In 3GFT, residue H61 was mutated back to Q61 to represent the wild type K-Ras and the GppNHp was modified to GDP to mimic the effect of the hydrolysis of the γ-phosphate. In addition to two end points, 20 replicas linking the start and the end points were generated using nudged elastic band (NEB) method (please see the following section). Thus, 22 systems were used as the initial structures for explicit solvent molecular dynamic (MD) simulations.

1.2 Nudged Elastic Band (NEB) Method

To dissect the Ras deactivation process, NEB method[2-3], a powerful tool to probe the transition pathway of protein dynamics was carried out. In NEB, a series of replicas, referred to as "images" of the system under study, are created and connected to each other with strings and they form a discrete representation of the path from the start, GTP-bound active state, to the end, GDP-bound inactive state. Energy minimization of the overall system, but with the start and the end structures fixed, generates a minimum energy path (MEP). Each replica between the start and the end is connected to the previous and the next by "springs" along the MEP, which can maintain the replicas from sliding down the energy landscape onto the adjacent replicas. In NEB, as shown in Eq. (1), the total force F on each replica, i, is decoupled into a parallel force, $F_i^{\parallel}$,and a perpendicular force, $F_i^{\perp}$, by the tangent vector. $F_i^{\parallel}$ accounts for the artificial springs connecting each replica (Eq. (2)), where k_i equals to the spring constant between replica P_i and P_{i+1}, and P is the 3N dimensional position vector of replica i, and $\boldsymbol{\tau}$ is the 3N dimensional tangent unit vector describing the path. $F_i^{\perp}$ is calculated by subtracting out the parallel component from F, as shown in Eq. (3), where $\nabla V(P_i)$ is the energy gradient with respect to the atomic coordinates in the whole system in replica i.

$$F_i = F_i^{\parallel} + F_i^{\perp} \quad (1)$$

$$F_i^{\parallel} = [(k_{i+1}(P_{i+1} - P_i)) - k_i(P_i - P_{i-1})) \cdot \tau]\tau \quad (2)$$

$$F_i^{\perp} = -\nabla V(P_i) + ((\nabla V(P_i)) \cdot \tau)\tau \quad (3)$$

In NEB calculation, the K-Ras in the active form (PDB ID: 3GFT), with GppNHp modified into GDP, and K-Ras in the inactive form (PDB ID: 4LPK) were referred to as the start and end points. The modified AMBER FF03 force field in AMBER 14 was assigned to K-Ras and the general AMBER force field (GAFF) was used to treat the GDP[4,5]. K-Ras systems were first solvated using the TIP3P water model and counterions were added to maintain electroneutrality of the systems. Then, 20 replicas were created, which stretch along the Active→Inactive pathway and were connected to each other by strings. Neighbouring replicas were first fit to each other using RMSD (root means square deviation) with respect to the backbone atoms within the corresponding systems. Then, NEB force decoupling was applied to the backbone atoms in each replica. During the heating stage from 0 to 300K, the spring force was set to 10 kcal mol^{-1} $Å^{-2}$ with a Langevin collision frequency of 1000 ps^{-1}, while in the following simulated annealing, equilibrium and slow cooling processes, a larger spring force of 50 kcal mol^{-1} $Å^{-2}$ was used. The simulated annealing method was employed for the optimization of the pathway from active state to the inactive state and it was carried out based on previously reported workflow[6,7].

1.3 MD Simulations

MD simulations were carried out with AMBER 14. Modified AMBER ff03 force field[4,5] was applied to the K-Ras protein and GDP was treated with the general AMBER force field (GAFF) and its related parameters were obtained from the AMBER parameter database (www.pharmacy.manchester.ac.uk/bryce/amber). The overall systems were first solvated in truncated octahedral boxes with the TIP3P water molecules and were neutralized with counterions. Then, the complex systems were subject to two-round energy minimization. In the first step, the protein scaffolds were restrained and a 5000-step maximum minimization cycle was carried out and in the second step, the whole systems were minimized without any restrictions. Subsequently, the systems were heated from 0 K to 300 K within 300 ps, and equilibration at 300 K

for 700 ps followed, both of which were under a positional restraint of 10 kcal mol^{-1} $Å^{-2}$ in a canonical ensemble (NVT). Finally, for 22 initial structures (the start and the end points and 20 replicas inserted by NEB method), each was performed 10 independent MD runs with random initial velocities. 200-ns MD simulations were carried out for each system, which resulted in 220 independent trajectories with a cumulation of 44-μs length. The particle mesh Ewald method[8] was employed for the incorporation of the long-range electrostatic interactions within the systems and a 10 Å cutoff was introduced for the short-range electrostatics and van der Waals interactions. All covalent bonds engaging hydrogen atoms were restricted using the SHAKE method.

Section 2: The Choice of Two Metrics to Project the Simulation Data to Obtain the Conformational Landscape of Ras Deactivation

Structural superimposition of the crystal structures of GppNHp- and GDP-bound Ras yields a root-mean square deviation (RMSD) of 1.91 Å for all of the backbone atoms. The overlapped structures show that the most significant conformational differences between the two structures are derived from the switch I and switch II domains (Figure 1C). If the switch I and switch II domains are excluded in the calculation, the backbone RMSD is 0.58 Å for all of the backbone atoms between the remaining elements of the two structures, further supporting the notion that the major conformational differences between GppNHp- and GDP-bound Ras are localized to the switch I and II domains. Notably, in the GppNHp-bound state, Tyr32 on the switch I domain is in the "up" conformation, denoted as "$Tyr32_{up}$", and the α2-helix on the switch II domain is positioned in the "inward" conformation, denoted as "$\alpha2\text{-}helix_{in}$" (Figure 1D). In contrast, in the GDP-bound state, Tyr32 on the switch I domain is in the "down" conformation, denoted as "$Tyr32_{down}$", and the α2-helix on the switch II domain is positioned in the "outward" conformation, denoted as "$\alpha2\text{-}helix_{out}$" (Figure 1D). Based on this observation, we chose the following two order parameter pairs to project the simulation data to obtain the conformational landscape. One is defined by the distance (d) from the hydroxyl oxygen of the switch I residue Tyr32 to the Cα atom of the P loop residue Gly12, which reflects the conformational changes of the switch I domain, and the other is defined by the dihedral (φ) calculated by the Cα atoms of Ile24 (α1-helix), Ala66 (α2-helix), Glu76 (α2-helix), and Val81 (β4), which monitors the conformational rotations of the α2-helix of the switch II domain. Furthermore, crystallography data were projected onto the reaction path sampled by MD simulations and their distributions are similar (Figure 2B), indicating the reasonable agreement between them. Therefore, it is feasible to choose the two order parameter pairs (d and φ) to project the simulation data to obtain the conformational landscape.

Section 3: Convergence Test of the Free Energy Landscape Using Different Simulations Datasets

To confirm that our MD simulations are sufficient to construct a reliable free energy landscape, we assessed the convergence of the free energy landscape by choosing different subsets from the complete simulation dataset. Six subsets of the complete dataset were extracted with different accumulated simulation times by truncated each MD simulation into varied length, namely 33 μs (220×150 ns) (Figure S1A), 35.2 μs (220×160 ns) (Figure S1B), 37.4 μs (220×170 ns) (Figure S1C), 39.6 μs (220×180 ns) (Figure S1D), 41.8 μs (220×190 ns) (Figure S1E), and 44 μs (220×200 ns) (Figure S1F). To check whether the sampling is converged or not, we projected the MD snapshots from each subset onto the same two order parameters. As shown in Figure S1, all datasets demonstrate similar free energy landscapes and no extra metastable state appears while increasing the simulation time, suggesting that the current timescale of MD simulations is enough to explore the major substates of the Ras deactivation pathway.

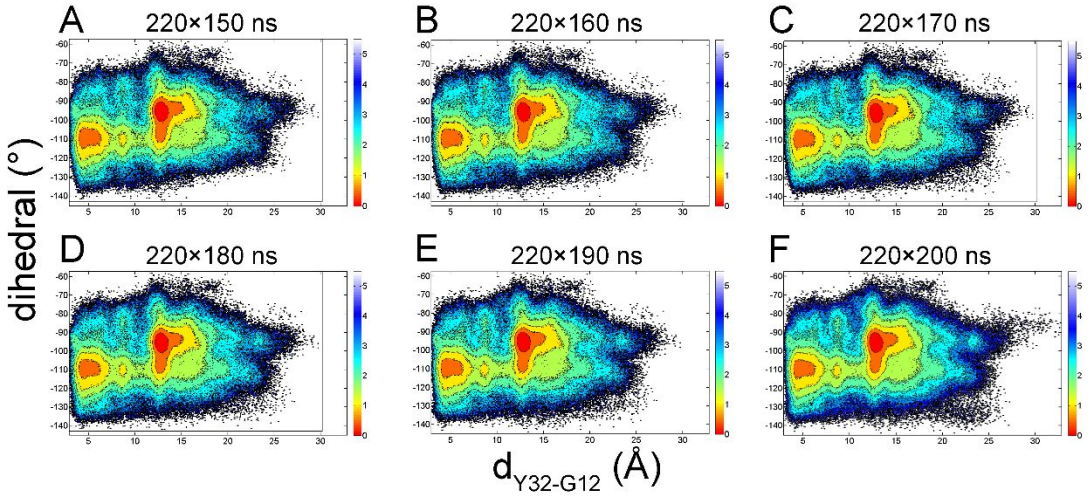

Figure S1. Projections of different subsets of the complete simulation dataset onto the two same order parameters (unit in *kcal/mol*), with the aggregated time of 33 μs (A), 35.2 μs (B), 37.4 μs (C), 39.6 μs (D), 41.8 μs (E), and 44 μs (F).

Section 4: Comparison of Intermediate State with the Active and Inactive states of Ras

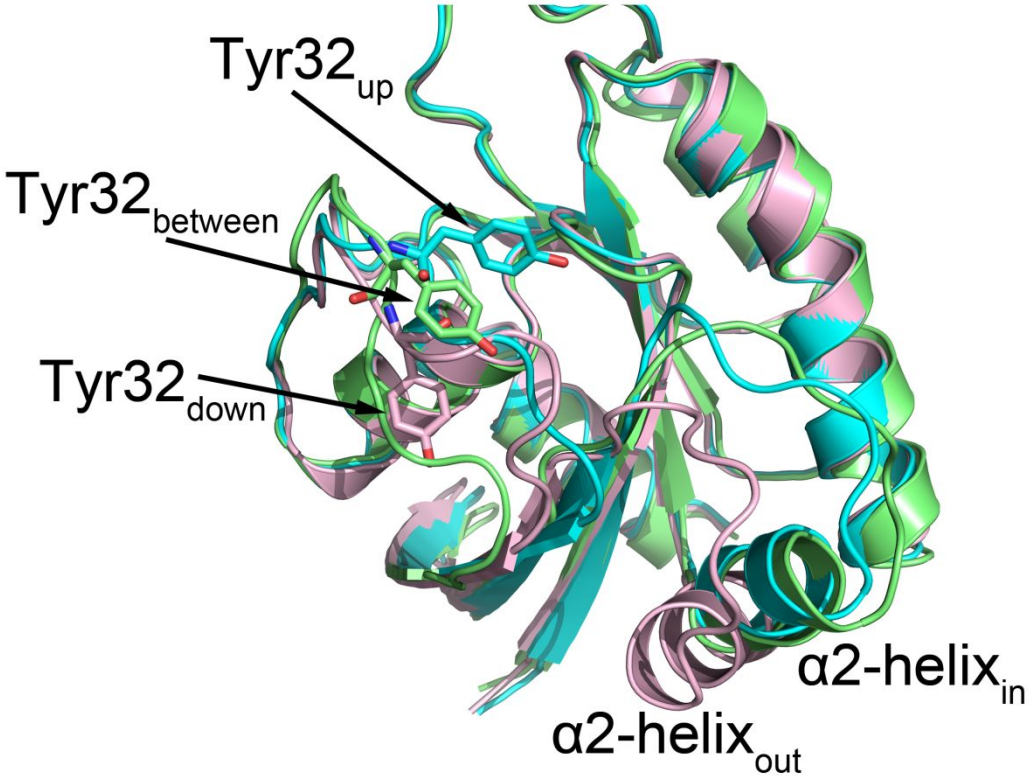

Figure S2. Stepwise deactivation process of Ras. Representative structures captured by MD simulations of active (cyan), intermediate (green), and inactive (pink) states of Ras. Tyr32 is represented by stick models and it exhibits "up"→"between"→"down" transitions along the Ras deactivation path. The α2-helix stays still in the "α2-helix$_{in}$" conformation from the active to the intermediate states. It is positioned at the "α2-helix$_{out}$" conformation in the inactive form of Ras.

Section 5: Comparing Our Intermediate State Obtained from MD Simulations with the Proposed Intermediates Determined by Crystallography

Currently, crystal structures of two Ras mutants (A59G and Q61G) whose structures have proposed to resemble the intermediates in the conformational transition from Ras-GTP to Ras-GDP. The two mutations (A59G and Q61G) are located at the N-terminal switch II domain. The resulting mutations lead to the enhanced flexibility of the switch II domain, facilitating the conformational variation of switch II domain.

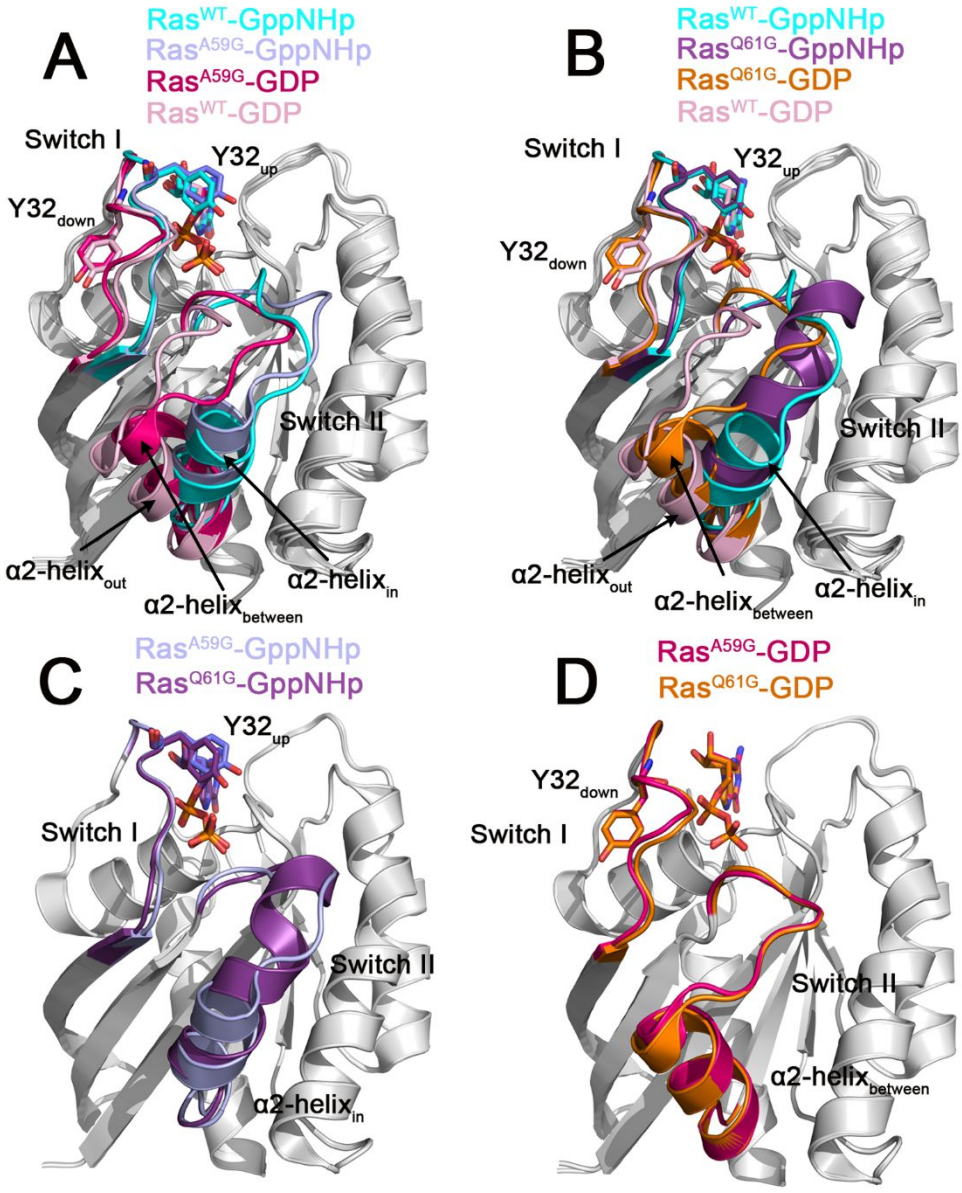

Figure S3. (A) Cartoon representation of the backbone superimposition of crystal structures of Ras^{WT}-GppNHp (PDB ID 6GOD, cyan), Ras^{WT}-GDP (PDB ID 4LPK, pink), Ras^{A59G}-GppNHp (PDB ID 1LF0, light blue), and Ras^{A59G}-GDP (PDB ID 1LF5, red). (B) Cartoon representation of the backbone superimposition of crystal structures of Ras^{WT}-GppNHp (PDB ID 6GOD, cyan), Ras^{WT}-GDP (PDB ID 4LPK, pink), Ras^{Q61G}-GppNHp (PDB ID 1ZW6, purple), and Ras^{Q61G}-GDP (PDB ID 1ZVQ, orange). Cartoon representation of the backbone superimposition of crystal structures of Ras^{A59G} and Ras^{Q61G} in the GppNHp- (C) and GDP-bound (D) states. The significant conformational differences of the switch I and II domains are colored correspondingly, the remaining elements showing less conformational changes colored by gray. Residue Tyr32, GppNHp, and GDP are depicted by stick models.

In the Ras^{A59G} mutant, crystal structures of Ras^{A59G} bound to GppNHp (Ras^{A59G}-GppNHp) (PDB ID 1LF0) and GDP (Ras^{A59G}-GDP) (PDB ID 1LF5) were determined, respectively. As shown in Figure S3A, backbone superimposition of crystal structures of Ras^{A59G}-GppNHp and Ras^{A59G}-GDP onto those of Ras^{WT}-GppNHp and Ras^{WT}-GDP shows that the switch I domain in the GppNHp- and GDP-bound Ras^{A59G} states adopts a conformation similar to that observed in the Ras^{WT} states, respectively; in contrast, the switch II domain in the Ras^{A59G} mutant shows different conformational variations compared to the Ras^{WT} state. In the GppNHp-bound state, the switch I domain in the Ras^{A59G}-GppNHp state adopts a conformation similar to that observed in the Ras^{WT}-GppNHp state. However, in the GDP-bound state, the α2-helix of the switch II domain exhibits a significant conformational change that is in the "between" conformation (denoted as "$\alpha2\text{-helix}_{between}$"), which is positioned between the "$\alpha2\text{-helix}_{in}$" in the active GTP-bound state and the "$\alpha2\text{-helix}_{out}$" in the inactive GDP-bound state.

In the Ras^{Q61G} mutant, crystal structures of Ras^{Q61G} bound to GppNHp (Ras^{Q61G}-GppNHp) (PDB ID 1ZW6) and GDP (Ras^{Q61G}-GDP) (PDB ID 1ZVQ) were determined, respectively. Figure S3B shows backbone superimposition of crystal structures of Ras^{Q61G}-GppNHp and Ras^{Q61G}-GDP onto those of Ras^{WT}-GppNHp and Ras^{WT}-GDP. Similar to the Ras^{A59G} mutant, the switch I domain in the GppNHp- and GDP-bound

Ras^{Q61G} as well as the switch II domain in the GppNHp-bound Ras^{Q61G} adopt similar conformations observed in the Ras^{WT}-GppNHp and Ras^{WT}-GDP states. The α2-helix of the switch II domain in the Ras^{Q61G}-GDP is also in the "$\alpha2\text{-helix}_{between}$" conformation.

Backbone superimposition of crystal structures of Ras^{A59G}-GppNHp and Ras^{Q61G}-GppNHp (Figure S3C) shows that the switch I domain of Ras^{A59G} and Ras^{Q61G} in the GppNHp-bound state is similar, while residues 61−64 of the N-terminal switch II region form an additional short 3_{10} helix that extends α2-helix by one turn in the Ras^{Q61G}-GppNHp compared to that in the Ras^{A59G}-GppNHp. Figure S3D shows backbone superimposition of crystal structures of Ras^{A59G}-GDP and Ras^{Q61G}-GDP. Both conformations of the switch I and II domains in the Ras^{A59G} and Ras^{Q61G} are identical in the GDP-bound state.

To further reveal the differences between our identified intermediate obtained from MD simulations and the proposed intermediates (A59G and Q61G) by crystallography, we superimposed the structures of our identified intermediate, Ras^{A59G}-GDP, and Ras^{Q61G}-GDP onto those of Ras^{WT}-GppNHp and Ras^{WT}-GDP states. As shown in Figure S4, the residue Tyr32 of the switch I domain in our identified intermediate is in the "between" conformation ($Y32_{between}$), which is different from that in the crystal structures of Ras^{A59G}-GDP and Ras^{Q61G}-GDP where it is in the "down" conformation ($Y32_{down}$) in both structures similar observed in the crystal structure of Ras^{WT}-GDP. However, the α2-helix of the switch II domain in our identified intermediate is still in the "inward" conformation ($\alpha2\text{-helix}_{in}$) similar observed in the crystal structure of Ras^{WT}-GppNHp, which is different from that in the crystal structures of Ras^{A59G}-GDP and Ras^{Q61G}-GDP where it is in the "between" conformation ($\alpha2\text{-helix}_{between}$) in both structures.

Based on above analyses, our identified intermediate is markedly different from crystal structures of Ras^{A59G} and Ras^{Q61G} along the reaction path of Ras hydrolysis. Our identified intermediate represents a conformational state where the switch I domain is in the "between" conformation along the reaction path, while the conformational transition of the switch II domain is not to start. However, both crystal structures of Ras^{A59G} and Ras^{Q61G} in the GDP-bound state represent a conformational state where the

conformational transition of the switch I domain is fully completed, while the transition of the switch II domain is in the "between" conformation along the reaction path. Therefore, our identified intermediate precedes the structures of Ras^{A59G}-GDP and Ras^{Q61G}-GDP along the reaction path of Ras hydrolysis.

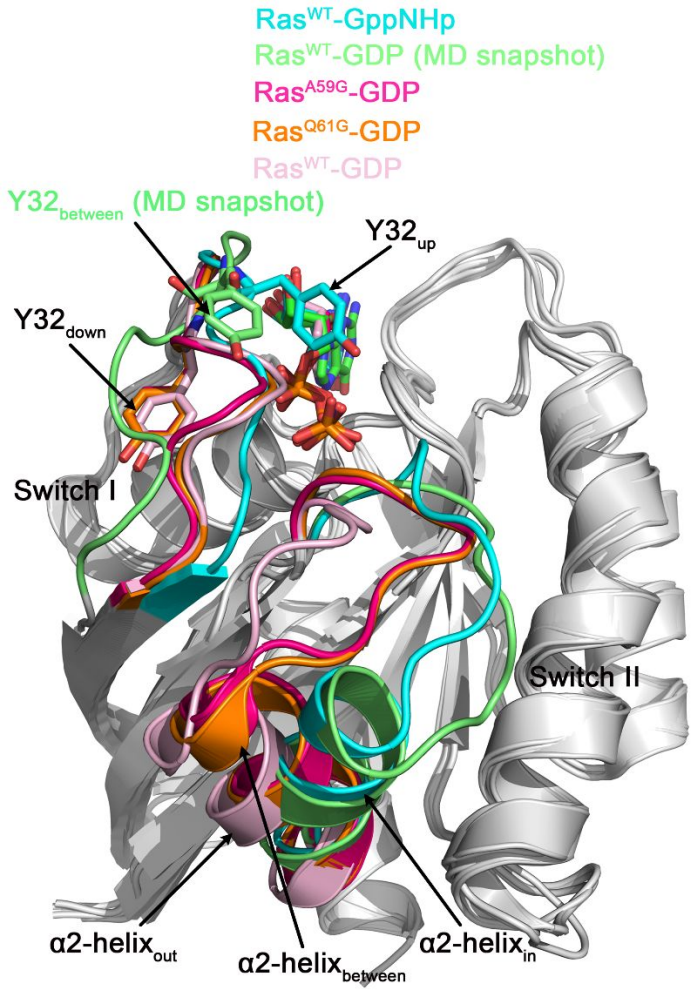

Figure S4. Cartoon representation of the backbone superimposition of structures of Ras^{WT}-GppNHp (PDB ID 6GOD, cyan), Ras^{WT}-GDP (PDB ID 4LPK, pink), Ras^{WT}-GDP (our identified intermediate, green), Ras^{A59G}-GDP (PDB ID 1LF5, red), and Ras^{Q61G}-GDP (PDB ID 1ZVQ, orange). The significant conformational differences of the switch I and II domains are colored correspondingly, the remaining elements showing less conformational changes colored by gray. Residue Tyr32, GppNHp, and GDP are depicted by stick models.

Section 6: Analysis of Reported Ras Structures

Table S1. Structures of Ras proteins

PDB IDs[a]	Isoforms	Methods	Resolution (Å)	Residue Number	Mutations	Nucleotide	Binding Partners	Ligands	Distance (Å)[b]	Dihedral (°)[c]	Ref
2N9C	N-Ras	Solution NMR		20							9
5UHV	N-Ras	X-Ray Diffration	1.672	166		GppNHp		GOL, Mg^{2+}	8.8	-107.542	10
3CON	N-Ras	X-Ray Diffration	1.649	190		GDP		Mg^{2+}	14.5	-93.474	To be published
5YXZ	K-Ras	X-Ray Diffration	1.7	170	G12C, C51S, C80L, C118S	GDP		Mg^{2+}, EDO, 94C	14.5	-88.827	To be published
5YY1	K-Ras	X-Ray Diffration	1.69	170	G12C, C51S, C80L, C118S	GDP		Mg2+, EDO, 94F	13.3	-104.379	To be published
5V9U	K-Ras	X-Ray Diffration	1.38	170	G12C, C51S, C80L, C118S	GDP		91S, GOL, Ca^{2+}	14.4	-107.488	11
6ARK	K-Ras	X-Ray Diffration	1.75	170	G12C, C51S,	GDP		BQD, GOL, Mg^{2+}	14	-76.612	12

					C80L, C118S						
6ASA	K-Ras	X-Ray Diffraction	2.545	168	D33E	GDP		Mg^{2+}	17.4	-90.648	13
6ASE	K-Ras	X-Ray Diffraction	1.554	170	A59G	GDP		Mg^{2+}	17	-91.156	13
6BP1	K-Ras	X-Ray Diffraction	2.001	169	A59G	GCP			17.1	-91.417	13
5UK9	K-Ras	X-Ray Diffraction	1.887	166		GDP		GOL, Mg^{2+}, GCP	13.2	-81.353	14
5WHA	K-Ras	X-Ray Diffraction	2.04	170	G12V	GDP	miniprotein 225-11	Ca^{2+}, Mg^{2+}	No Structure	-106.714	15
5WHB	K-Ras	X-Ray Diffraction	2.18	170	G12V	GDP	Ras binder peptide: 225-11 (A30R)	Ca^{2+}, Mg^{2+}	No Structure	-106.385	15
5WHD	K-Ras	X-Ray Diffraction	1.641	170	G12V, D38P	GDP			17.9	-107.773	15
5WHE	K-Ras	X-Ray Diffraction	1.91	170	G12V, D38P	GppNHp		Ca_{2+}, Mg^{2+}	25.9	-107.528	15

5WLB	K-Ras	X-Ray Diffraction	1.72	166	G12V	GppNHp	225-15 a, 225-15 b	SO_4^{2-}, PG4, Mg^{2+}	No Structure	-106.136	[15]
5WPM	K-Ras	X-Ray Diffraction	1.72	166	G12V	GppNHp	Ras binding peptide	SO_4^{2-}, Mg^{2+}	No Structure	No Structure	[15]
5MLA	K-Ras	X-Ray Diffraction	2.19	169		GSP	darpin k55	SO_4^{2-}, Mg^{2+}	12.7	-107.256	To be published
5MLB	K-Ras	X-Ray Diffraction	3.22	169		GDP	DARPin K27	Mg^{2+}	13.8	-88.231	To be published
5VP7	K-Ras	X-Ray Diffraction	1.7	170	G12A, C118S	GDP		Na^{+}, Mg^{2+}, PGE	14.1	-86.445	[16]
5VPI	K-Ras	X-Ray Diffraction	1.62	170	G12A, C118S	GTP		Mg^{2+}	4.1	114.118	[16]
5VPY	K-Ras	X-Ray Diffraction	2	170	G12A, C118S	GppNHp		Mg^{2+}, PG4	14.5	101.34	[16]
5VPZ	K-Ras	X-Ray Diffraction	1.85	170	G12A, C118S	GSP		Mg^{2+}	14.7	-98.772	[16]
5VQ0	K-Ras	X-Ray Diffraction	2.3	170	G12A, C118S	GDP		Mg^{2+}	13.9	-89.599	[16]

5VQ1	K-Ras	X-Ray Diffraction	1.78	170	Q61A, C118S	GDP		Mg^{2+}, PG4	13.9	-85.85	16
5VQ2	K-Ras	X-Ray Diffraction	1.96	170	C118S	GTP		Mg^{2+}	14.5	-92.916	16
5VQ6	K-Ras	X-Ray Diffraction	1.99	170	C118S	GSP		Mg^{2+}	14.7	-95.132	16
5VQ8	K-Ras	X-Ray Diffraction	2.3	170	C118S	GDP		Mg^{2+}	14.1	-86.27	16
5W22	K-Ras	X-Ray Diffraction	1.762	170	C118S	GDP		Mg^{2+}	13.9	-84.555	16
5VBM	K-Ras	X-Ray Diffraction	1.49	170	C51S, M72C, C80L, C118S	GDP		Mg^{2+}, 92V	14.2	-81.843	17
5V71	K-Ras	X-Ray Diffraction	2.228	169	G12C	GDP		Mg^{2+}, 8ZG	13.9	-75.184	18
5V9L	K-Ras	X-Ray Diffraction	1.981	169	G12C	GDP		Mg^{2+}, 91D	14	-77.552	19
5V9O	K-Ras	X-Ray Diffraction	1.56	169	G12C	GDP		Mg2+, 91G	13.6	-112.675	19

5UFE	K-Ras	X-Ray Diffraction	2.302	166		GppNHp	R11.1.6	Cl^-, Ca^{2+}, Mg^{2+}, Co^{2+}, Cd^{2+}	15.6	-109.619	20
5UFQ	K-Ras	X-Ray Diffraction	2.199	166	G12D	GppNHp	R11.1.6	Cl^-, Ca^{2+}, Mg^{2+}, Cd^{2+}	18.4	-108.795	20
5O2S	K-Ras	X-Ray Diffraction	3.22	169		GDP	DARPin K27	Mg^{2+}	13.8	-88.231	21
5O2T	K-Ras	X-Ray Diffraction	2.19	169		GSP	darpin 55	SO42-, Mg^{2+}	12.7	-107.256	21
5V6S	K-Ras	X-Ray Diffraction	1.7	170	G12C, C51S, C80L, C118S	GDP		8YD, Mg^{2+}	14.9	-102.84	22
5V6V	K-Ras	X-Ray Diffraction	1.72	170	G12C, C51S, C80L, C118S	GDP		8YA, GOL, Ca^{2+}	14.7	-113.595	22
5XCO	K-Ras	X-Ray Diffraction	1.25	171	G12D	GDP	Cyclic inhibitory peptide	EDO	14.7	-81.987	23
5KYK	K-Ras	X-Ray Diffraction	2.702	169	G12C			6ZD	19	-104.608	24

5UQW	K-Ras	X-Ray Diffraction	1.5	189	G12C	GDP		Mg^{2+}	13.3	-79.542	25
5US4	K-Ras	X-Ray Diffraction	1.83	189	G12D	GDP		GOL, Mg^{2+}	13.8	-85.258	25
5USJ	K-Ras	X-Ray Diffraction	1.94	189	G12D	GppNHp			3.9	-108.219	25
5TAR	K-Ras	X-Ray Diffraction	1.9	185		GDP	PDE-delta	FAR, EDO	18.7	-101.127	26
5TB5	K-Ras	X-Ray Diffraction	2	185		GDP	PDE-delta	FAR, EDO	No Structure	-100.675	26
5F2E	K-Ras	X-Ray Diffraction	1.4	170	G12C, C51S, C80L, C118S, R151G, E153D, Q165K, Y166H, R167K, L168E	GDP		GLY, GOL, 5UT, Mg^{2+}	13.4	No Structure	27
4QL3	K-Ras	X-Ray Diffraction	1.041	170	G12R	GDP		Mg^{2+}	13.2	-106.312	28

4TQ9	K-Ras	X-Ray Diffraction	1.49	169	G12V	GDP		Mg^{2+}	13.2	-106.497	28
4TQA	K-Ras	X-Ray Diffraction	1.13	169	G13D	GDP		Mg^{2+}	13.3	-106.793	28
4WA7	K-Ras	X-Ray Diffraction	1.986	170	Q61L	GDP		Mg^{2+}	13.9	-77.194	28
4PZY	K-Ras	X-Ray Diffraction	1.88	170	G12V, Q70C, C118S	GDP		2XR, Mg^{2+}	13.2	-102.017	29
4PZZ	K-Ras	X-Ray Diffraction	1.403	170	G12V, S39C, C118S	GDP		2XO, Mg^{2+}	13.6	-106.972	29
4Q01	K-Ras	X-Ray Diffraction	1.291	169	G12V, S39C, C118S	GDP		2XH, Mg^{2+}	14.2	-104.143	29
4Q02	K-Ras	X-Ray Diffraction	1.702	170	G12V, S39C, C118S	GDP		2XG, Mg^{2+}	13.1	-104.828	29
4Q03	K-Ras	X-Ray Diffraction	1.201	170	G12V, S39C, C118S	GDP		2XE, Mg^{2+}	13.5	-105.577	29
4LDJ	K-Ras	X-Ray Diffraction	1.15	170	G12C	GDP		Mg^{2+}	13.3	-106.916	30

4NMM	K-Ras	X-Ray Diffraction	1.89	170	G12C			Y9Z, Mg^{2+}	13.1	-106.56	30
4OBE	K-Ras	X-Ray Diffraction	1.24	170		GDP		Mg^{2+}	13.2	-105.908	30
4L8G	K-Ras	X-Ray Diffraction	1.521	170	G12C	GDP		Na^{+}, Mg^{2+}	14.2	-85.865	1
4LPK	K-Ras	X-Ray Diffraction	1.5	170		GDP		Na^{+}, Ca^{2+}	14.6	-77.321	1
4LRW	K-Ras	X-Ray Diffraction	2.151	170	C51S, C80L, C118S	GDP		Mg^{2+}	13.9	-77.728	1
4LUC	K-Ras	X-Ray Diffraction	1.29	170	G12C, C51S, C80L, C118S	GDP		Ca^{2+}, 20G	14.8	-107.648	1
4LV6	K-Ras	X-Ray Diffraction	1.5	170	G12C, C51S, C80L, C118S	GDP		Ca^{2+}, 20H	14.8	-106.875	1
4LYF	K-Ras	X-Ray Diffraction	1.568	170	G12C, C51S, C80L, C118S	GDP		21C	No Structure	-92.101	1

4LYH	K-Ras	X-Ray Diffraction	1.371	170	G12C, C51S, C80L, C118S	GDP		21F, SO_4^{2-}	No Structure	-92.157	1
4LYJ	K-Ras	X-Ray Diffraction	1.927	170	G12C, C51S, C80L, C118S	GDP		21F, Mg^{2+}	7.8	-105.216	1
4M1O	K-Ras	X-Ray Diffraction	1.571	170	G12C, C51S, C80L, C118S	GDP		21J	No Structure	-92.977	1
4M1S	K-Ras	X-Ray Diffraction	1.552	170	G12C, C51S, C80L, C118S	GDP		21K	No Structure	-94.232	1
4M1T	K-Ras	X-Ray Diffraction	1.703	170	G12C, C51S, C80L, C118S	GDP		21M	No Structure	-92.331	1
4M1W	K-Ras	X-Ray Diffraction	1.58	170	G12C, C51S, C80L, C118S	GDP		21R, Mg^{2+}	No Structure	-91.801	1
4M1Y	K-Ras	X-Ray Diffraction	1.491	170	G12C, C51S, C80L, C118S	GDP		21S	No Structure	-92.669	1

4M21	K-Ras	X-Ray Diffraction	1.94	170	G12C, C51S, C80L, C118S	GDP		21Y	No Structure	-94.466	1
4M22	K-Ras	X-Ray Diffraction	2.09	170	G12C, C51S, C80L, C118S	GDP		22C, Mg^{2+}	14.6	-116.257	1
4EPR	K-Ras	X-Ray Diffraction	2	170	G12D, C118S	GDP		Mg^{2+}	13.8	-84.666	31
4EPT	K-Ras	X-Ray Diffraction	2	170	C118S	GDP		Mg^{2+}, 0QW	13.9	-106.278	31
4EPV	K-Ras	X-Ray Diffraction	1.35	170	C118S	GDP		Mg^{2+}, 0QX	14	-106.534	31
4EPW	K-Ras	X-Ray Diffraction	1.7	170	C118S	GDP		Mg^{2+}, 0QV	13.1	-105.491	31
4EPX	K-Ras	X-Ray Diffraction	1.76	170	G12V, C118S	GDP		Mg^{2+}, 0QR	13.3	-106.444	31
4EPY	K-Ras	X-Ray Diffraction	1.801	170	G12V, C118S	GDP		Mg^{2+}, 0QY	14	-107.046	31
4DSN	K-Ras	X-Ray Diffraction	2.03	189	G12D	GCP		Mg^{2+}, EDO	4.1	-108.277	32

4DSO	K-Ras	X-Ray Diffraction	1.85	189	G12D	GSP		Mg^{2+}, GOL, BEN	4.2	-107.824	32
4DST	K-Ras	X-Ray Diffraction	2.3	189	G12D	GCP		9LI, ACT, GOL, EDO, Mg^{2+}, DMS	4.3	-108.439	32
4DSU	K-Ras	X-Ray Diffraction	1.7	189	G12D	GDP		BZI, Mg^{2+}	15	-101.68	32
3GFT	K-Ras	X-Ray Diffraction	2.27	187	Q61H	GppNHp		CIT, Mg^{2+}	4.1	-108.186	To be published
5P21	H-Ras	X-Ray Diffraction	1.35	166		GppNHp		Mg^{2+}	9	-117.041	33
1Q21	H-Ras	X-Ray Diffraction	2.2	171		GDP		Mg^{2+}	13.2	-114.775	34
2Q21	H-Ras	X-Ray Diffraction	2.2	171	G12V	GDP		Mg^{2+}	12.7	-113.309	34
4Q21	H-Ras	X-Ray Diffraction	2	189		GDP		Mg^{2+}	13	-85.409	35

6Q21	H-Ras	X-Ray Diffraction	1.95	171		GCP		Mg^{2+}	15.7	-97.436	35
121P	H-Ras	X-Ray Diffraction	1.54	166		GCP		Mg^{2+}	8.9	-115.414	To be published
221P	H-Ras	X-Ray Diffraction	2.3	166	D38E	GppNHp		Mg^{2+}	9.2	-116.197	36
421P	H-Ras	X-Ray Diffraction	2.2	166	G12R	GppNHp		Mg^{2+}	9	-119.123	36
521P	H-Ras	X-Ray Diffraction	2.6	166	G12V, A59T	GTP		Mg^{2+}	9.7	-118.624	36
621P	H-Ras	X-Ray Diffraction	2.4	166	Q61H	GppNHp		Mg^{2+}	8.9	-116.869	36
721P	H-Ras	X-Ray Diffraction	2	166	Q61L	GppNHp		Mg^{2+}	8.9	-114.695	36
821P	H-Ras	X-Ray Diffraction	1.5	166	G12P	GppNHp		Mg^{2+}	8.9	-112.644	37
1AGP	H-Ras	X-Ray Diffraction	2.3	166	G12D	GppNHp		Mg^{2+}	4.8	-105.688	37
1CRP	H-Ras	Solution NMR		166		GDP		Mg^{2+}	13.7	-95.064	38

1CRR	H-Ras	Solution NMR		166		GDP		Mg^{2+}	16.2	-98.502	38
1CRQ	H-Ras	Solution NMR		166		GDP		Mg^{2+}	15.4	-96.047	38
1PLJ	H-Ras	X-Ray Diffraction	2.8	166	G12P	CAG		Mg^{2+}	8.6	No Structure	39
1PLK	H-Ras	X-Ray Diffraction	2.8	166		GTP		Mg^{2+}	13	-109.995	39
1PLL	H-Ras	X-Ray Diffraction	2.8	166	G12P	GDP			16.2	-105.531	39
1GNP	H-Ras	X-Ray Diffraction	2.7	166		AGN		Mg^{2+}	9	-113.439	40
1GNQ	H-Ras	X-Ray Diffraction	2.5	166		CAG		Mg^{2+}	13	-112.735	40
1GNR	H-Ras	X-Ray Diffraction	1.85	166		CAG		Mg^{2+}	8.1	-111.868	40
1JAH	H-Ras	X-Ray Diffraction	1.8	166	G12P	GCP		Mg^{2+}	9	-107.452	41
1JAI	H-Ras	X-Ray Diffraction	1.8	166	G12P	GCP		Mn^{2+}	9	-105.571	41

1AA9	H-Ras	Solution NMR		171		GDP		Mg^{2+}	13	-109.805	42
1WQ1	H-Ras	X-Ray Diffraction	2.5	166		GDP	P120GAP	Mg^{2+}, AF3	9.4	-112.41	43
1BKD	H-Ras	X-Ray Diffraction	2.8	166			SON OF SEVENLESS-1		15.8	-112.32	44
1LFD	H-Ras	X-Ray Diffraction	2.1	167	E31K	GppNHp	RALGDS	Mg^{2+}	9	-106.625	45
1CLU	H-Ras	X-Ray Diffraction	1.7	166	G12P	DBG		Mg^{2+}	No Structure	-114.431	46
1RVD	H-Ras	X-Ray Diffraction	1.9	166	G12V	DBG		Mg^{2+}	No Structure	-112.687	46
1QRA	H-Ras	X-Ray Diffraction	1.6	166		GTP		Mg^{2+}	8.7	-106.726	47
1CTQ	H-Ras	X-Ray Diffraction	1.26	166		GppNHp		Mg^{2+}	8.8	-105.45	47
1HE8	H-Ras	X-Ray Diffraction	3	166	G12V	GppNHp	PI3KCG	Mg2+	4.8	-107.341	48
1IAQ	H-Ras	X-Ray Diffraction	2.9	166	T35S	GppNHp		Mg^{2+}	No Structure	No Structure	49

1IOZ	H-Ras	X-Ray Diffraction	2	171		GDP			14.3	-106.153	50
1K8R	H-Ras	X-Ray Diffraction	3	166		GppNHp	Protein kinase byr2	Mg^{2+}	4.5	-105.797	51
1LF0	H-Ras	X-Ray Diffraction	1.7	166	A59G	GppNHp		Mg^{2+}, Ca^{2+}	4.2	-107.406	52
1LF5	H-Ras	X-Ray Diffraction	1.7	166	A59G	GDP		Mg^{2+}	13.9	-83.719	52
1NVU	H-Ras	X-Ray Diffraction	2.2	166	A59G	GTP	SON OF SEVEN LESS PROTEIN HOMOLOG 1	Mg^{2+}, PO_4^{3-}	4.3	-110.702	53
1NVV	H-Ras	X-Ray Diffraction	2.18	166	Y64A	GppNHp	SON OF SEVEN LESS PROTEIN HOMOLOG 1	Mg^{2+}, PO_4^{3-}	4.3	-107.688	53
1NVW	H-Ras	X-Ray Diffraction	2.7	166		GppNHp	SON OF SEVEN LESS	Mg^{2+}, PO_4^{3-}	4.2	-109.762	53

							PROTEIN HOMOLOG 1				
1NVX	H-Ras	X-Ray Diffraction	3.2	166	A59G	GTP	SON OF SEVENLESS PROTEIN HOMOLOG 1	Mg^{2+}, PO_4^{3-}	4.3	-111.45	53
1P2S	H-Ras	X-Ray Diffraction	2.45	166		GppNHp		Mg^{2+}, ETF	9.1	-106.407	54
1P2T	H-Ras	X-Ray Diffraction	2	166		GppNHp		Mg^{2+}	9	-97.552	54
1P2U	H-Ras	X-Ray Diffraction	2	166		GppNHp		Mg^{2+}, IPA	9.1	-97.29	54
1P2V	H-Ras	X-Ray Diffraction	2.3	166		GppNHp		Mg^{2+}, HEZ	9	-105.149	54
1XD2	H-Ras	X-Ray Diffraction	2.7	166	Y64A	GDP	SON OF SEVENLESS PROTEIN	Mg^{2+}, PO_4^{3-}	4.7	-105.468	55

							HOMOLOG 1				
1XCM	H-Ras	X-Ray Diffraction	1.84	167	G60A	GppNHp		Mg^{2+}	17.8	-91.023	To be published
1XJ0	H-Ras	X-Ray Diffraction	1.7	166	G60A	GDP		Mg^{2+}	14	-84.618	To be published
2C5L	H-Ras	X-Ray Diffraction	1.9	173	G12V	GTP	PLCE1	Mg^{2+}, GOL	4.6	-107.492	[56]
1ZVQ	H-Ras	X-Ray Diffraction	2	166	Q61G	GDP		Mg^{2+}	13.8	-84.253	[57]
1ZW6	H-Ras	X-Ray Diffraction	1.5	166	Q61G	GppNHp		Mg^{2+}, Ca^{2+}	4.1	-110.91	[57]
2CL6	H-Ras	X-Ray Diffraction	1.24	166	Y32C, C118S	CAG		XY2, Mg^{2+}	Mutated	-110.102	[58]
2CL7	H-Ras	X-Ray Diffraction	1.25	166	Y32C, C118S	GTP		XY2, Mg^{2+}	Mutated	-111.162	[58]
2CLC	H-Ras	X-Ray Diffraction	1.3	166	Y32C, C118S	GTP		XY2, Mg^{2+}	Mutated	-110.894	[58]
2EVW	H-Ras	X-Ray Diffraction	1.05	166	Y32C, C118S	CAG		XY2, Mg^{2+}	Mutated	-112.666	[58]

2CL0	H-Ras	X-Ray Diffraction	1.8	166	Y32C, C118S	GppNHp		XY2, Mg^{2+}, TRS	Mutated	-86.226	58
2CLD	H-Ras	X-Ray Diffraction	1.22	166	C118S	GDP		Mg^{2+}	No Structure	-113.162	58
2CE2	H-Ras	X-Ray Diffraction	1	166	Y32C, C118S	GDP		XY2, Mg^{2+}	Mutated	-87.804	58
2UZI	H-Ras	X-Ray Diffraction	2	166	G12V	GTP	ANTI-RAS FV LIGHT AND HEAVY CHAINS	Mg^{2+}, Zn^{2+}	4.7	-105.906	59
2QUZ	H-Ras	X-Ray Diffraction	1.49	166	K117R	GDP		Mg^{2+}	13.8	-84.468	60
2RGA	H-Ras	X-Ray Diffraction	1.9	166	Q61I	GppNHp		Mg^{2+}, Ca^{2+}	4	-94.427	61
2RGB	H-Ras	X-Ray Diffraction	1.35	166	Q61K	GppNHp		Mg^{2+}, Ca^{2+}	4	-94.762	61
2RGC	H-Ras	X-Ray Diffraction	1.6	166	Q61V	GppNHp		Mg^{2+}, Ca^{2+}	4	-95.552	61

2RGD	H-Ras	X-Ray Diffraction	2	166	Q61L	GppNHp		Mg2+, Ca2+	4	-93.478	61
2RGE	H-Ras	X-Ray Diffraction	1.4	166		GppNHp		Mg^{2+}, Ca^{2+}	4.2	-110.149	61
2RGG	H-Ras	X-Ray Diffraction	1.45	166	Q61I	GppNHp		Mg^{2+}	8.8	-106.771	61
2VH5	H-Ras	X-Ray Diffraction	2.7	166	G12V	GTP	ANTI-RAS FV LIGHT AND HEAVY CHAINS	Mg^{2+}, Zn^{2+}	4.8	-105.911	62
3DDC	H-Ras	X-Ray Diffraction	1.8	166	D30E, E31K	GppNHp	Rassf5	Mg^{2+}	4.5	-104.267	63
3I3S	H-Ras	X-Ray Diffraction	1.36	166	T50I	GppNHp		Mg^{2+}, Ca^{2+}	4.2	-96.275	64
2X1V	H-Ras	X-Ray Diffraction	1.7	166	I163F	GDP			No Structure	No Structure	To be published
3K8Y	H-Ras	X-Ray Diffraction	1.3	166		GppNHp		Mg^{2+}, Ca^{2+}, ACT	4.3	-108.41	65

3K9N	H-Ras	X-Ray Diffraction	2	166	Y32F	GppNHp		Mg^{2+}, Ca^{2+}	Mutated	-106.557	65
3LBH	H-Ras	X-Ray Diffraction	1.85	166		GppNHp		Mg^{2+}, Ca^{2+}, ACT	4.1	-108.359	65
3LBI	H-Ras	X-Ray Diffraction	2.087	166		GppNHp		Mg^{2+}, Ca^{2+}, ACT	3.9	-108.25	65
3LBN	H-Ras	X-Ray Diffraction	1.862	166		GppNHp		Mg^{2+}, Ca^{2+}	4.2	-108.153	65
3LO5	H-Ras	X-Ray Diffraction	2.568	166	S17N	GDP		Ca^{2+}, PO_4^{3-}	19.6	-102.407	66
3KUD	H-Ras	X-Ray Diffraction	2.15	166		GDP	RAF1	Mg^{2+}	4.1	-101.641	67
3KKM	H-Ras	X-Ray Diffraction	1.7	172	T35S	GppNHp		Mg^{2+}, SO_4^{2-}	13.6	-103.053	68
3KKN	H-Ras	X-Ray Diffraction	2.09	172	T35S	GppNHp		Mg^{2+}	17.6	-91.76	68
3K9L	H-Ras	X-Ray Diffraction	1.8	166	Y32F	GppNHp		Mg^{2+}, Ca^{2+}	Mutated	No Structure	To be published

3OIU	H-Ras	X-Ray Diffraction	1.32	166	Q61L	GppNHp		Mg^{2+}, Ca^{2+}, ACT	4	-107.839	69
3OIV	H-Ras	X-Ray Diffraction	1.837	166	G12V	GppNHp		Mg^{2+}, Ca^{2+},DTT	4.9	-97.17	69
3OIW	H-Ras	X-Ray Diffraction	1.3	166	G12V	GppNHp		Mg^{2+}, Ca^{2+}, ACT	5	-108.549	69
3L8Y	H-Ras	X-Ray Diffraction	2.02	166		GppNHp		Mg^{2+}, Ca^{2+}, Zn^{2+}, YCN	3.8	-103.08	70
3L8Z	H-Ras	X-Ray Diffraction	1.44	166		GppNHp		Mg^{2+}, Ca^{2+}	4	-109.068	70
3RRY	H-Ras	X-Ray Diffraction	1.6	166		GppNHp		Mg^{2+}, Ca^{2+}	3.9	-94.116	71
3RRZ	H-Ras	X-Ray Diffraction	1.6	166		GppNHp		Mg^{2+}, Ca^{2+}, GOL	4.2	-94.42	71
3RS0	H-Ras	X-Ray Diffraction	1.4	166		GppNHp		Mg^{2+}, Ca^{2+}, YEG	4	-94.982	71
3RS2	H-Ras	X-Ray Diffraction	1.836	166		GppNHp		Mg^{2+}, Ca^{2+}, ETF	3.9	-95.832	71

3RS3	H-Ras	X-Ray Diffraction	1.52	166		GppNHp		Mg^{2+}, Ca^{2+}, HEX	3.9	-95.508	71
3RS4	H-Ras	X-Ray Diffraction	1.7	166		GppNHp		Mg^{2+}, Ca^{2+}, HEZ	4.1	-95.998	71
3RS5	H-Ras	X-Ray Diffraction	1.68	166		GppNHp		Mg^{2+}, Ca^{2+}, DMF	4	-92.903	71
3RS7	H-Ras	X-Ray Diffraction	1.7	166		GppNHp		Mg^{2+}, Ca^{2+}	4.2	-96.152	71
3RSL	H-Ras	X-Ray Diffraction	1.7	166		GppNHp		Mg^{2+}, Ca^{2+}, RSF	4.1	-105.069	71
3RSO	H-Ras	X-Ray Diffraction	1.6	166		GppNHp		Mg^{2+}, Ca^{2+}, RSG	4	-94.741	71
2LCF	H-Ras	Solution NMR		172	T35S	GppNHp		Mg^{2+}	8.4	-102.77	72
3TGP	H-Ras	X-Ray Diffraction	1.3075	166		GppNHp		Mg^{2+}	9	No Structure	73
4EFL	H-Ras	X-Ray Diffraction	1.9	171		GppNHp		Mg^{2+}	17.6	-91.743	74
4EFM	H-Ras	X-Ray Diffraction	1.9	171	G12V	GppNHp		Mg^{2+}	17.7	-91.769	74

4EFN	H-Ras	X-Ray Diffraction	2.3	171	Q61L	GppNHp		Mg^{2+}	17.6	-91.923	74
3V4F	H-Ras	X-Ray Diffraction	1.391	166		GppNHp		Mg^{2+}, Ca^{2+}, DTU	3.9	-95.626	75
4DLR	H-Ras	X-Ray Diffraction	1.319	166		GppNHp		Mg^{2+}, Ca^{2+}, DTU	3.8	-96.26	75
4DLS	H-Ras	X-Ray Diffraction	1.819	166		GppNHp		Mg^{2+}, Ca^{2+}	4.1	No Structure	75
4DLT	H-Ras	X-Ray Diffraction	1.699	166		GppNHp		Mg^{2+}, Ca^{2+}, ACT	3.9	-108.327	75
4DLU	H-Ras	X-Ray Diffraction	1.6	166		GppNHp		Mg^{2+}, Ca^{2+}, ACT	4.1	-108.752	75
4DLV	H-Ras	X-Ray Diffraction	1.572	166		GppNHp		Mg^{2+}, Ca^{2+}, DTT	4	-94.72	75
4DLW	H-Ras	X-Ray Diffraction	1.72	166		GppNHp		Mg^{2+}, Ca^{2+}, ACT	4	-108.704	75
4DLX	H-Ras	X-Ray Diffraction	1.731	166		GppNHp		Mg^{2+}, Ca^{2+}, DTU	3.9	-95.431	75

4DLY	H-Ras	X-Ray Diffraction	1.57	166		GppNHp		Mg^{2+}, Ca^{2+}, DTT	3.9	-95.904	75
4DLZ	H-Ras	X-Ray Diffraction	1.662	166		GppNHp		Mg^{2+}, Ca^{2+}, DTU	4	-95.583	75
2LWI	H-Ras	Solution NMR		172	T35S	GppNHp		Mg^{2+}, KOB	11.4	-103.539	76
4G0N	H-Ras	X-Ray Diffraction	2.45	166		GppNHp	RAF1	Mg^{2+}, Ca^{2+}, DTU, ACT	4.1	-107.969	77
4G3X	H-Ras	X-Ray Diffraction	3.25	166	Q61L	GppNHp	RAF1	Mg^{2+}	3.2	-107.963	77
4K81	H-Ras	X-Ray Diffraction	2.4	171	G12V	GTP	GRB14	Mg^{2+}, GOL	5	-106.683	78
4L9S	H-Ras	X-Ray Diffraction	1.606	171	G12C	GDP		Mg^{2+}, Ca^{2+}, Na^{+}	4	-95.583	1
4L9W	H-Ras	X-Ray Diffraction	1.952	171	G12C	GppNHp		Mg^{2+}, Ca^{2+}	4.2	-108.142	1
4NYI	H-Ras	X-Ray Diffraction	2.9612	167	Y64A	GppNHp	SON OF SEVEN LESS PROTEIN	Mg^{2+}, 2PX	4	-109.313	79

							HOMOLOG 1				
4NYJ	H-Ras	X-Ray Diffraction	2.8522	166	Y64A	GppNHp	SON OF SEVENLESS PROTEIN HOMOLOG 1	Mg^{2+}, 2PZ	4.1	-111.414	[79]
4NYM	H-Ras	X-Ray Diffraction	3.5529	166	Y64A	GppNHp	SON OF SEVENLESS PROTEIN HOMOLOG 1	Mg^{2+}, RND	4.3	-109.904	[79]
4URU	H-Ras	X-Ray Diffraction	2.83	185			SON OF SEVENLESS PROTEIN HOMOLOG 1	6W2	16.3	-110.768	[80]
4URV	H-Ras	X-Ray Diffraction	2.58	185			SON OF SEVENLESS PROTEIN	FMT, UMK	16.2	-111.289	[80]

							HOMOLOG 1				
4URW	H-Ras	X-Ray Diffraction	2.76	185			SON OF SEVENLESS PROTEIN HOMOLOG 1	DXO	16	-111.616	80
4URX	H-Ras	X-Ray Diffraction	2.49	185			SON OF SEVENLESS PROTEIN HOMOLOG 1	FMT, FK1, HXY	16.1	-111.306	80
4URY	H-Ras	X-Ray Diffraction	2.47	185			SON OF SEVENLESS PROTEIN HOMOLOG 1	RV1	16	-112.227	80
4URZ	H-Ras	X-Ray Diffraction	2.24	185			SON OF SEVENLESS PROTEIN	VJP	16	-112.339	80

							HOMOLOG 1				
4US0	H-Ras	X-Ray Diffraction	2.17	185			SON OF SEVENLESS PROTEIN HOMOLOG 1	NEQ	16.1	-111.131	[80]
4US1	H-Ras	X-Ray Diffraction	2.65	185			SON OF SEVENLESS PROTEIN HOMOLOG 1	L71	16.1	-111.326	[80]
4US2	H-Ras	X-Ray Diffraction	2.48	185			SON OF SEVENLESS PROTEIN HOMOLOG 1	L7S	16.1	-111.299	[80]
4XVQ	H-Ras	X-Ray Diffraction	1.887	166	Y137E	GppNHp		Mg^{2+}, GOL	8.7	-114.441	[81]
4XVR	H-Ras	X-Ray Diffraction	2.031	166	Y137F	GppNHp		Mg^{2+}, Ca^{2+}	8.8	-102.198	[81]

2N42	H-Ras	Solution NMR		172	T35S				9.8	-78.466	82
2N46	H-Ras	Solution NMR		172	T35S				10.1	-103.784	82
4RSG	H-Ras	Neutron Diffraction	1.907	166		GppNHp		Mg^{2+}, DOD	9	-116.859	83
5B2Z	H-Ras	X-Ray Diffration	1.56	171		GppNHp		Mg^{2+}, Ca^{2+}	4.2	-96.488	84
5B30	H-Ras	X-Ray Diffration	1.6	171		GppNHp		Mg^{2+}, Ca^{2+}, Na^{+}	4.1	-115.704	84
5E95	H-Ras	X-Ray Diffration	1.402	168		GDP	Mb(NS1)	Mg^{2+}	15.2	-104.343	85
5WDO	H-Ras	X-Ray Diffration	1.65	170		GppNHp		Mg^{2+}, Ca^{2+}, Na^{+}	4.2	-107.073	86
5WDP	H-Ras	X-Ray Diffration	1.35	166	L120A	GppNHp		Mg^{2+}, Ca^{2+}	4.2	-107.637	86
5WDQ	H-Ras	X-Ray Diffration	1.25	170	L120A	GppNHp		Mg^{2+}, Ca^{2+}, Na^{+}, ACT	4	-96.296	86

5X9S	H-Ras	X-Ray Diffraction	2.5	192		GppNHp		Mg^{2+}, Ca^{2+}	4	-93.934	87
6AXG	H-Ras	X-Ray Diffraction	3.302	170			RASGRP4		18.3	-104.065	88
5VBE	H-Ras	X-Ray Diffraction	1.57	171	M72C	GDP		Mg^{2+}, 92V	13.9	-88.456	17
5VBZ	H-Ras	X-Ray Diffraction	2.2	171	M72C	GppNHp		Mg^{2+}, 92V	4.2	-101.955	17
6AMB	H-Ras	X-Ray Diffraction	2.5	170		GppNHp	Afdn	Mg^{2+}	3.7	-97.162	89
5WPL	H-Ras	X-Ray Diffraction	2.15	166	G12V	GppNHp	Ras-binding peptide	Mg^{2+}, Ca^{2+}	26	-107.329	15

[a] Some PDB files contain more than one Ras structures and they are all included in our study. In the table we only show the data for the first structure in every PDB file.

[b]Distance was calculated between the hydroxyl oxygen atom of Tyr32 and the Cα atom of Gly12. In some structures, Tyr32 was mutated or its side-chain conformation was unresolved, which are denoted as "Mutated" or "No Structure", respectively.

[c]Dihedral was calculated by the Cα atoms of Ile24, Ala66, Glu76 and Val81. In some structures, the involved residues were mutated or their side-chain conformations were unresolved. Instead, their nearby residues are used and some are denoted as "No Structure".

Section 7: Interactions between Thr35 and Gly60 with GTP and GDP

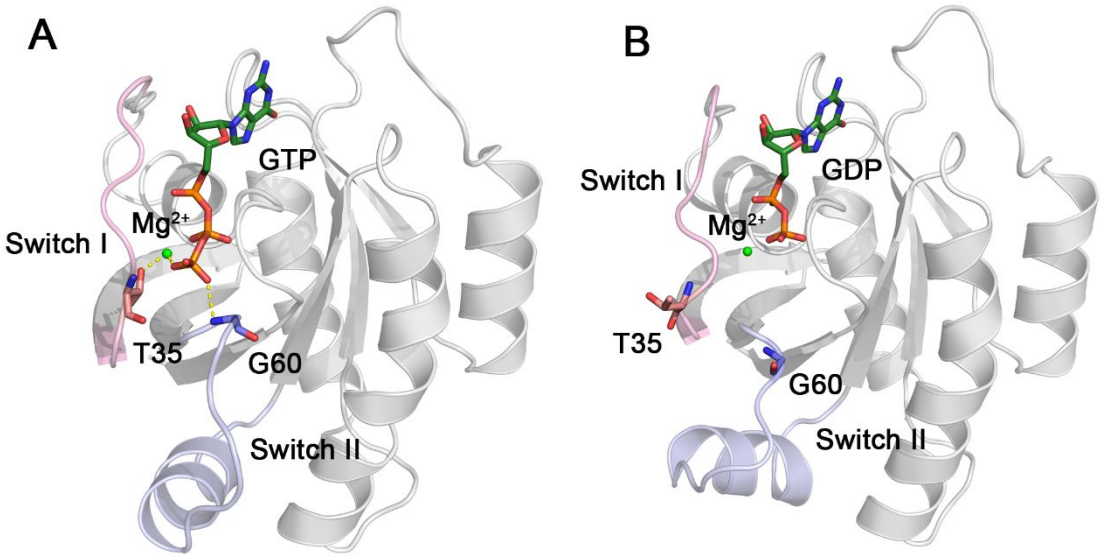

Figure S5. (**A**) Coupled interaction of Thr35 and Gly60 with the γ-phosphate of GTP (PDB ID: 6GOD). The backbone carbon atoms of Thr35 and Gly60 are colored in blue and the phosphorus atoms of GTP are colored in red. Interactions between Thr35 and Gly60 are depicted by yellow dash lines. **(B)** Uncoupling of Thr35 and Gly60 with GDP after hydrolysis (PDB ID: 4LPK). Ras is shown in gray with the switch I and II domains in pink, and light blue, respectively, and Mg^{2+} ion is displayed by a green sphere. Thr35, Gly60, and GTP/GDP are represented by sticks.

Section 8: Markov State Models (MSMs) Construction

Markov state models (MSMs) were built from our simulation data using MSMBuilder[90,91] following the standard protocol[90,92] (http://msmbuilder.org/3.8.0/). The first step for MSM construction is the transformation of the Cartesian coordinates from the raw simulation data into vector features invariant to translation and rotation. The "AlphaAngleFeaturizer" algorithm in MSMBuilder that extracts alpha (dihedral) angles was applied to the featurization of our simulation data. Then, to capture the slow and important conformation changes and to improve the statistical qualities of our data, dimensionality reduction was carried out using time-structure based independent component analysis (tICA).[93] For our alpha angle structural features, each was transformed into 10 tICA components. Next, the states of the MSM were defined by clustering the interconverting conformations. The "MiniBatchKMeans" algorithm for Mini-Batch K-Means clustering was used to partition the tICA data into clusters. Finally, a 200-microstate MSM with a lag time of 8 ns was created (please see the following section for details) and applied to further study.

Section 9: Validation of the Markovian lagtime for the Ras model

To examine whether our model was Markovian and reliable, we carried out implied timescales analysis. Multiple transition probability matrixes (TPMs), which account for the probabilities of transitions among all microstates, were constructed for different lag times (i.e. time intervals between transitions) and the relaxation timescales or the implied timescale was calculated from Eq. (4):

$$\tau_i = -\frac{\tau}{\ln \lambda_i} \quad (4)$$

where τ is the lag time for the construction of TPM, λ_i is the i^{th} eigenvalue of the TPM, and τ_i represents the implied timescale or the relaxation timescale corresponding to the i^{th} relaxation mode of the system. Markovian property can be demonstrated if τ_i is independent of τ, which can be depicted by a level-off implied timescales plot.

TPMs in MSM were computed with the lag times τ chosen from the set of values with the help of PyEMMA[94]. As shown in Figure S6, our implied timescales test shows that the plot levels off at lag times of 6 ns. Hence, for lag times approximately longer than 6 ns, the models are Markovian. Based on this, we choose a lag time of 8 ns and use it for further analysis. We then lumped our model into 9 macrostates using the Robust Perron Cluster Cluster Analysis (PCCA+) plugin implemented in MSMBuilder package and the resulting model was also demonstrated to be Markovian with Chapman-Kolmogorov test using PyEMMA (Figure S7).

In addition to implied timescales analysis, our MSMs were also tested against our simulation data and the experimental results. The 200-microstate MSM was projected onto the conformational landscape of Ras sampled by MD simulations and the microstates ensemble spanned across the Ras hydrolysis pathway (Figure S8), which indicates that our MSM is a good reflection of the deactivation process in reality. Moreover, all Ras structures reported so far are extracted from PDB and they are also projected onto the Ras deactivation path and their distribution resembles to that of the MSM (Figure S8), which suggests that the computational model is in reasonable agreement with the experimental data. Taken together, these agreements between

theory and experiment highlight the ability of our MSM to reproduce the overall Ras hydrolysis reaction under study and it is suitable for further investigation.

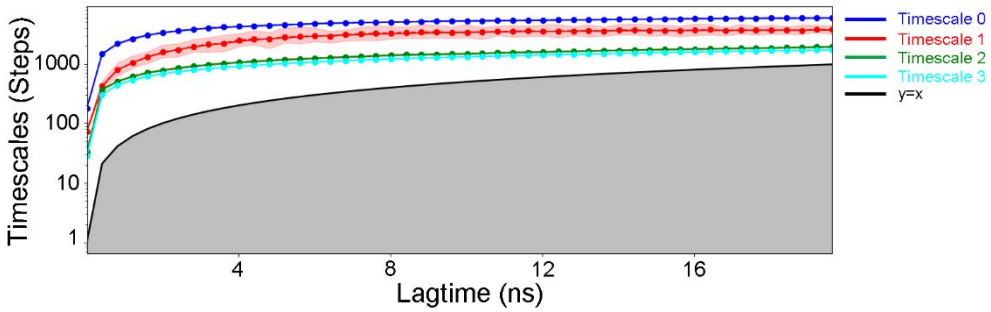

Figure S6. The implied timescale plots as a function of lag time for the MSMs constructed based on simulations data. The logarithmic convergence of the longest relaxation timescales suggested that the corresponding models were Markovian since the model kinetics were independent of the lagtimes.

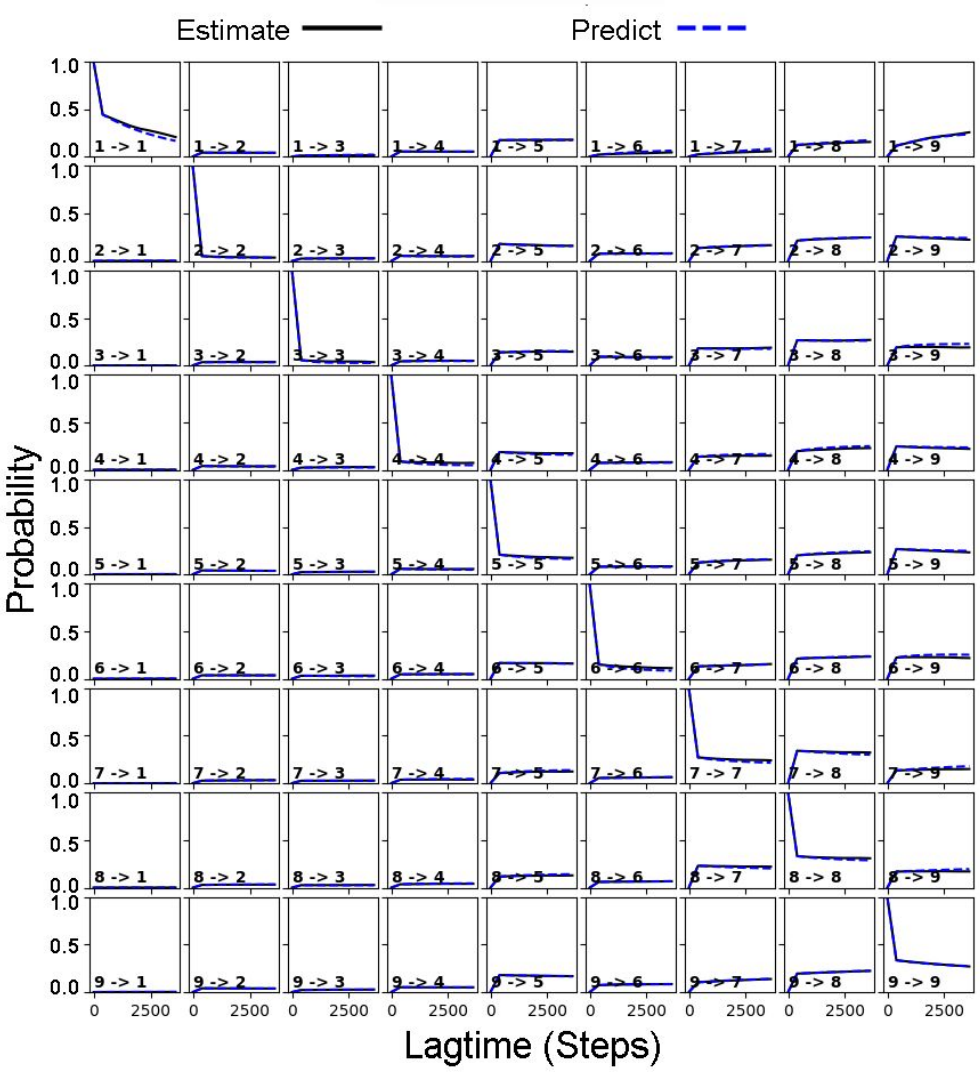

Figure S7. Validation of MSM through Chapman-Kolmogorov test. Shown are data for MSM (black line) and the observed trajectory (blue dotted line, with estimated error).

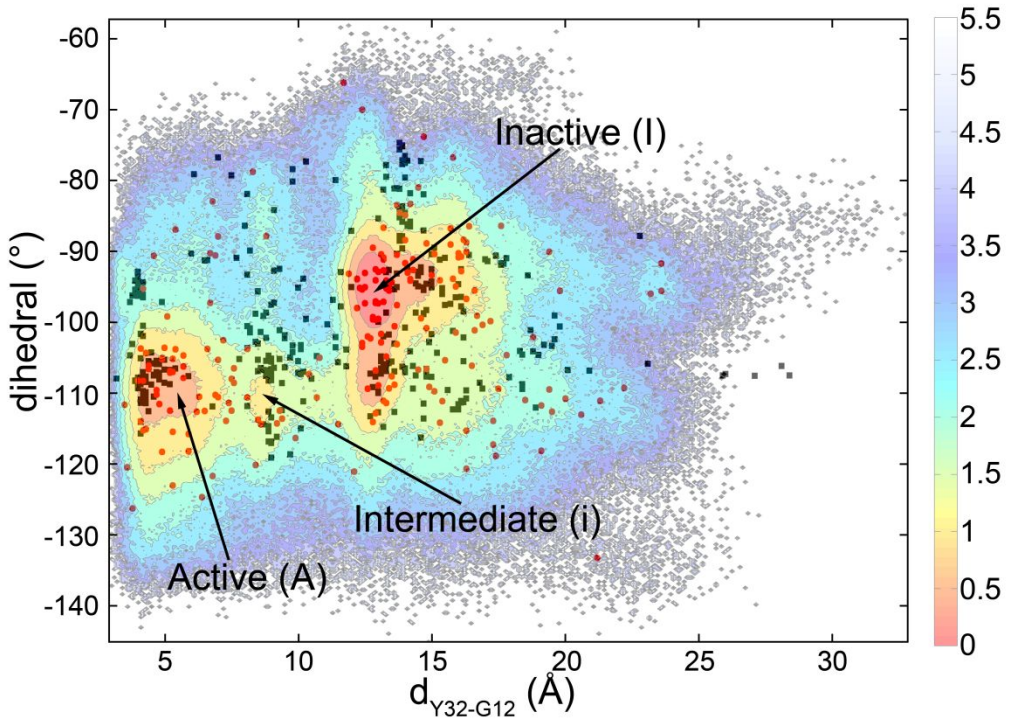

Figure S8. MSM and crystallographic results show similar distributions along the Ras deactivation path. Conformational landscape of the Ras deactivation is mapped by MD simulations. The $d_{Y32-G12}$ is defined as the distance between hydroxyl oxygen of Tyr32 and Cα of Gly12, and the dihedral is calculated by the Cα of Ile24, Ala66, Glu76 and Val81. Black dots represent the existing crystal structures of Ras and red dots represent MSM microstates.

Section 10: Extraction and Analysis of Representative Substate Structures

Following the standard protocol for time-structure based independent component analysis (tICA) and configurations extraction[90,92], we carried out tICA for our simulation data and MSMs. As shown in Figure S9, our trajectories were projected onto two dominant tICs and the representative substate structures were extracted from the low-free-energy regions and were denoted as S1-S9.

Projection of the representative configurations onto the Ras deactivation pathway shows that they distribute along the reaction path and can cover most of the critical states including the newly revealed intermediate state (Figure 2B). Also, they are tested against the existing crystallography results and they agree well with the closest crystal structures with root mean square deviations (RMSDs) of less than 1 Å (Table S2). Therefore, these results show that our MSM and the MSM-based substates are sufficiently good reflections of reality to carry out further research.

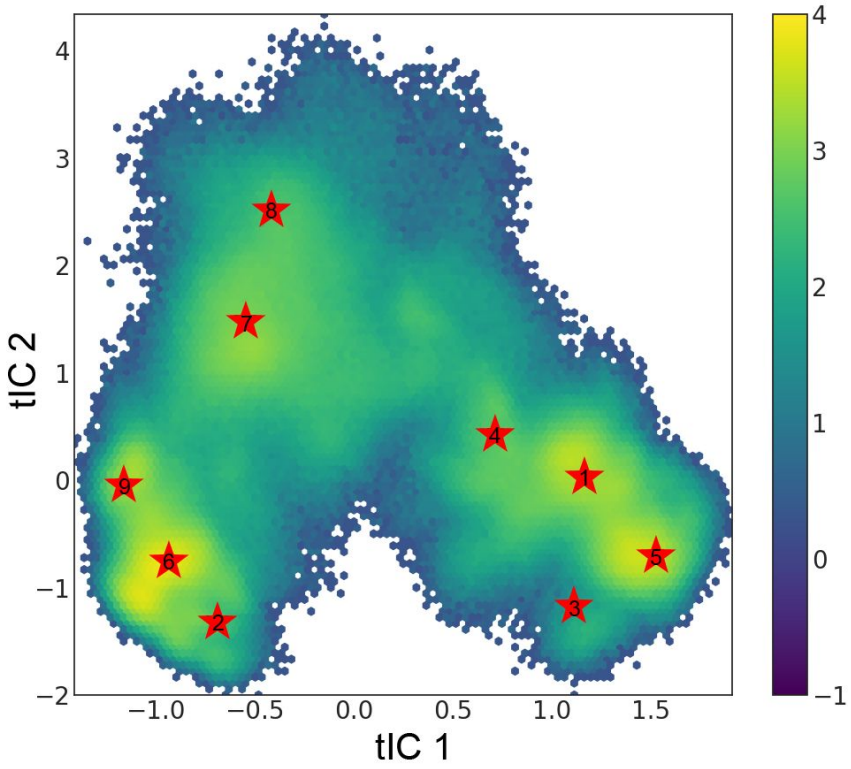

Figure S9. Projection of the MD simulations onto the two dominant modes of the tICA model in MSM analysis. The nine representative configurations, denoted as S1-S9 by red stars, were extracted from the model according to the centroids of the low-free-energy regions.

Table S2. Comparison between the nine MSM substate structures and their closest crystal structures

Substate ID	Distance (Å)[a]	Dihedral (°)[b]	PDB ID	Distance (Å)	Dihedral (°)	RMSD (Å)
S1	4.0	-108.242	5WDP	4.2	-107.637	0.706
S2	4.2	-95.262	2RGD	4.0	-93.478	0.870
S3	8.1	-110.610	1GNR	8.1	-111.868	0.857
S4	13.5	-107.629	4TQA	13.3	-106.793	0.725
S5	15.4	-111.160	5UFE	15.6	-109.619	0.735
S6	13.1	-102.846	4OBE	13.2	-105.908	0.884
S7	15.3	-94.094	6Q21	15.7	-97.436	0.930
S8	13.8	-84.553	5VQ8	14.1	-86.270	0.743
S9	13.4	-95.541	5UQW	13.3	-92.973	0.926

[a] distance is calculated between the hydroxyl oxygen atom of Tyr32 and the Cα atom of Gly12.

[b] dihedral is calculated by the Cα atoms of Ile24, Ala66, Glu76 and Val81.

Section 11: Kinetic Properties of Ras Deactivation

We calculated the mean first passage time (MFPT) for our MSM model in an attempt to explore the dynamic hydrolysis pathway. Details for the calculation of MFPTs from given MSMs have been reported by Singhal *et al.* previously[95-96], and here, we employed MSMbuilder package for the calculations.

MFPTs come as products of series or linear equations based on the transition probability matrix of the corresponding MSM model. Within the MSM, they represent the average time it takes to transit from state *i* to state *j*. MFPT is defined based on the following equations:

$$MFPT(i) = \sum_{transition(i,k)} Tik \times MFPT(i\,|transition(i,k)) \quad (5)$$

$$MFPT(i) = \sum_{edge(i,k)} Tik \times (\tau + MFPT(k)) \quad (6)$$

In equation (5), the sum goes over all transition from state *i* to state *j* and *Tik* stands for the probability to transit from state *i* to state *k*. In equation (6), the sum goes over all edges starting from state *i*, and τ stands for the time interval between state *i* and state *j*. We can further write equations for MFPT from all states to state *j*, and by combining these sets of linear equations, we can work out the results for *MFPT(i)*.

Our MSM indicates that the dominant deactivation pathway follows the sequential transitions in the order of S1→S3→S4→S6→S9 (Figure 2B). The kinetics of the deactivation pathway indicates that the transition from the active to inactive states is fast (approximately 600 ns) (Figure S10), which is in line with the relatively small energy barriers between the active, inactive and intermediate states observed in our free energy landscape plot shown in Figure 2A but is inconsistent with the experimental measurement characterized by slow intrinsic rate of GTP hydrolysis[52, 97-98]. However, there is one caveat worth mentioning owing to the different kinetics obtained by the MFPT calculation and the experimental observation. Our initial structures used in simulations obtained from the transition pathway generated by the MEP method have crossed the energy barriers between the conformational state transitions. Because of an extensive set of distinct initial structures of Ras deactivation used in simulations, its conformational landscapes could be rapidly sampled. Similar situation has also been

observed in Src kinase activation[99]. As a result, this factor must presumably affect the kinetics of Ras deactivation.

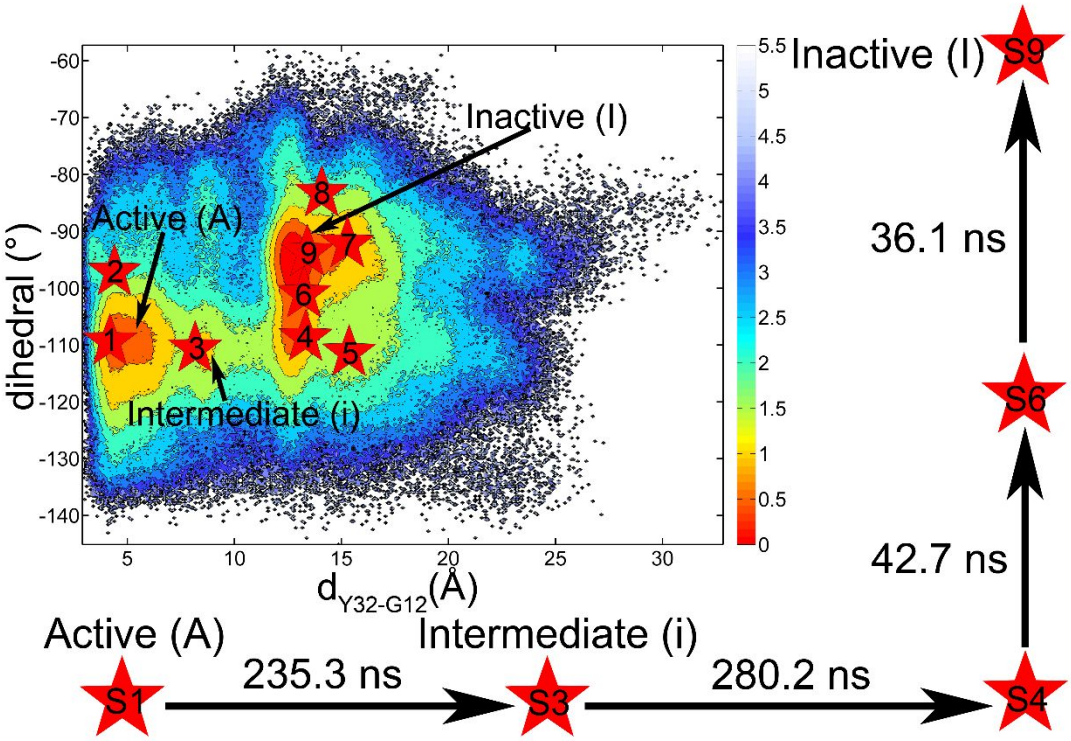

Figure S10. The kinetics transition pathway of Ras from Active state (A) to Inactive state (I) through the major MSM substates (S1→S3→S4→S6→S9), and the MFPTs for the transitions are provided above the arrows.

Section 12: Pocket Detection and Clustering

Fpocket was employed for pocket detection on our MSM substate structures[100,101]. All results were classified and clustered based on their conformations and sequences, yielding four groups designated as P1-P4 (Table S3).

Table S3. Fpocket prediction results and the corresponding classic binding sites on Ras

Fpocket Result	Predicted Sequence	Reported Site	Reported Region	Ligands	Crystal Structure	Pocket Similarity Score	Ref
P1	7-10,16,37,57-59,61-63,68,72,78,92,96,99,103	Switch II Pocket (S-IIP)	α4-helix (87-91), α5-helix (93-104), β1-sheet (3-9), loop 1 (10-15), and Switch II (59-76)	Ras^{G12C}-specific covalent inhibitors	5V9L	0.47493	19
P2	5-7,36-40,54-59,66,67,70,71,74-77	Kobe Site	β1-sheet (3-9), β3-sheet (38-46), β4-sheet (49-57), and Switch II (59-76)	DCAI[a], Kobe-family ligands, indole-, sulfonamide-, phenol-containing ligands	2LWI	0.62955	76
P3	76-78,100,104-106,108-110,162,163,166	Cyclen Site	α4-helix (87-91), α7-helix (152-167), β6-sheet (104-107), loop 10 (108-110), and loop 7 (74-78)	M^{2+}-cyelen, M^{2+}-bisphenol A[b]	3L8Y	0.58607	70
P4	16-21,24,25,29,30-32,34-36,38,40,55,57,59						

[a] DCAI stands for 4,6-dichloro-2-methyl-3-aminoethyl-indole.

[b] M^{2+} stands for bivalent metal ions.

Section 13: Comparison Analysis of Computational and Experimental Pocket Results

In our pocket detection results, P1-P3 were first compared with previous reported classic allosteric sites, Switch II pocket (S-IIP)[1], Kobe site[76], and cyclen site[70] by sequences and structures (Figure 3, Figure S11, Figure S12, and Table S3). Then, APoc (Alignment of Pockets), an algorithm for large-scale structural comparison of protein pockets[102], was applied to analyze the structural similarity of the computationally detected and experimentally determined sites (Table S3). Considering both the sequence and structure similarity and the relatively high Pocket Similarity (PS) scores, our MSM-based prediction outcomes and the existing experimental results can be regarded to be similar.

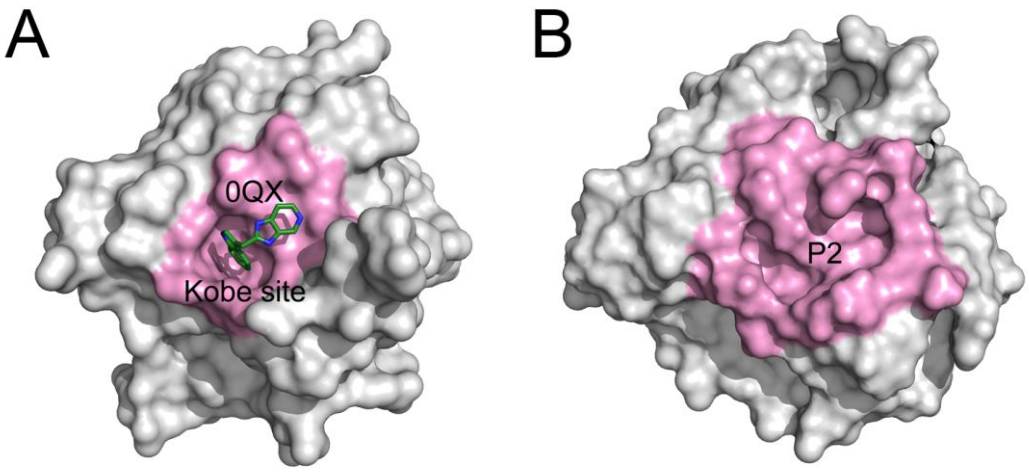

Figure S11. A. Structure of Kobe site in K-Ras with ligand 0QX inside (PDB ID: 4EPV). K-Ras is gray and Kobe site is highlighted in pink. Ligand 0QX is represented by sticks and colored by element, with the backbone carbon atoms shown in green. **B.** Structure of P2 predicted by MSM-based method. K-Ras is gray and P2 is highlighted in pink.

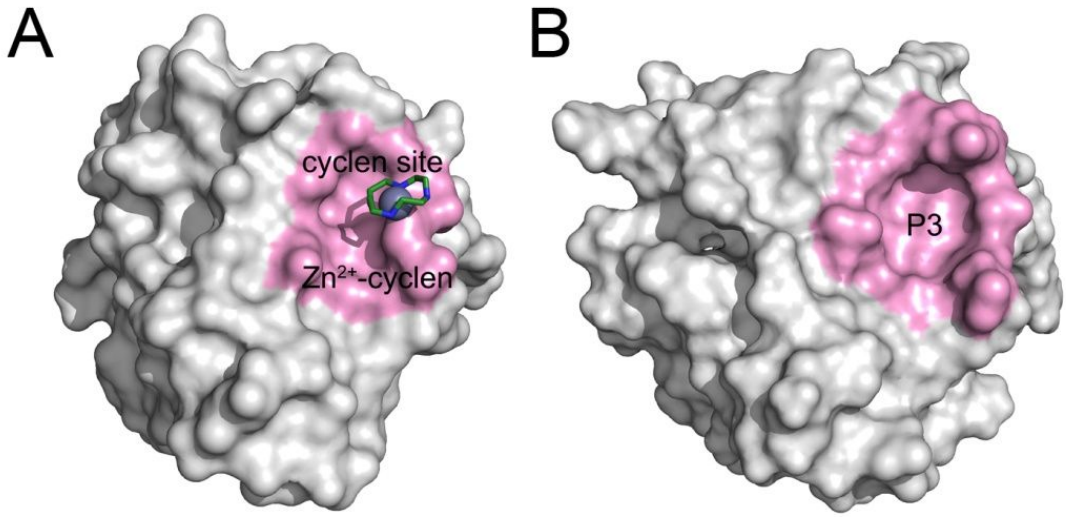

Figure S12. A. Structure of cyclen site in H-Ras in complex with ligand Zn^{2+}-cyclen (PDB ID: 3L8Y). H-Ras is gray and cyclen site is highlighted in pink. Ligand Zn^{2+}-cyclen is shown by sticks and the carbon atoms are shown in green. **B.** Structure of P3 predicted by MSM-based method. H-Ras is gray and P3 is highlighted in pink.

Section 14: The Dynamic Nature of S-IIP

The conformational transitions of Ras deactivation in our simulations suggest a dynamic nature of the SWII pocket. To test this hypothesis, we superimposed the crystal structures of Ras G12C with covalent inhibitors bound to the allosteric SIIP pocket (Figure S13). This comparison shows the different locations and topology of the SIIP pocket for covalent allosteric inhibitors. The different binding poses of covalent allosteric inhibitors highlight the flexible nature of the SIIP pocket. Therefore, the dynamic nature of the SIIP pocket observed in the simulations is consistent with the experimentally crystallographic studies.

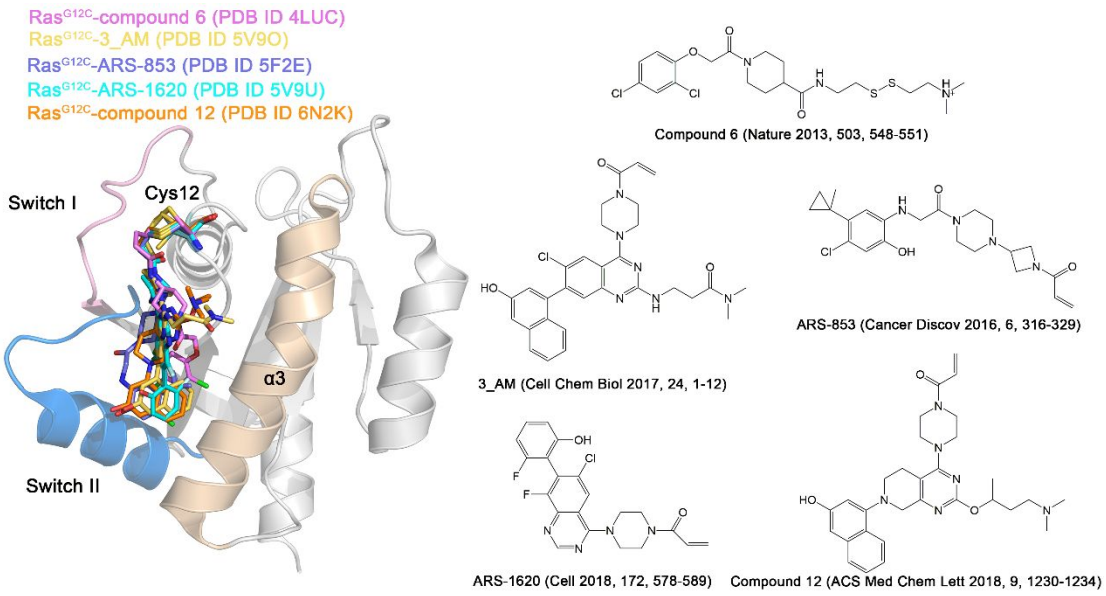

Figure S13. Representative covalent inhibitors bound to the allosteric switch II pocket (SIIP) of Ras^{G12C}. The crystal structure of Ras^{G12C}-compound **6** (carbon colored in pink) (PDB ID: 4NMM) is used as a template, and other crystal structures of K-Ras^{G12C} allele-specific allosteric covalent inhibitors, Ras^{G12C}-3_AM (carbon colored in yellow) (PDB ID: 5V9O), Ras^{G12C}-ARS-853 (carbon colored in light blue) (PDB ID: 5F2E), Ras^{G12C}-ARS-1620 (carbon coloured in cyan) (PDB ID: 5V9U), and Ras^{G12C}-compound **12** (carbon colored in orange) (PDB ID: 6N2K), are aligned to the template. The switch I and II domains and the α3-helix are colored in pink, light blue, and wheat, respectively. The mutated Cys12 and covalent inhibitors are depicted by stick models. The chemical structures of covalent inhibitors, compound **6**, 3_AM, ARS-853, ARS-1620, and compound **12**, are showing with their original sources.

Section 15: Protein-Protein Interactions (PPIs) Analysis for Ras and Comparison with the Newly Detected Pocket

PISA (Proteins, Interfaces, Structures and Assemblies) is a web server for the investigation of macromolecular complexes and structures and it can also provide detailed insights into the protein surfaces, interfaces and assemblies[103]. Here, PISA was applied to the analysis of the PPIs between Ras and its major effectors, Raf (PDB ID: 4G0N)[77], PI3K (PDB ID: 1HE8)[48], and RalGDS (PDB ID: 1LFD)[104]. Residues along the PPI surfaces are revealed and the interaction details are also unveiled. PISA analysis results are compared with P4 and the large overlap between the PPI interfacial residues and P4 implies that this pocket situates along the PPI interfaces, which is consistent with the structural comparisons (Figure 4). Additionally, residues involved in hydrogen bonds or salt bridges formation unraveled by PISA are regarded as hot-spots for PPIs (Figure S14) and most of them (Thr20, Ile21, Gln25, Glu31, Ile36, Asp38, and Ile55 are covered by P4 (Figure S15). Hence, P4 possesses great potential as a drug target for the modulation of the PPIs between Ras and its effector proteins.

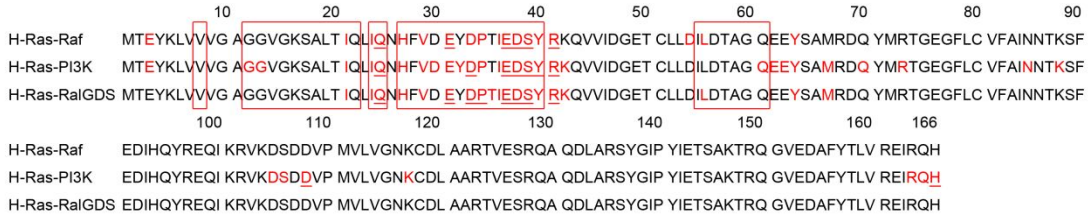

Figure S14. Sequence alignment of the residues on H-Ras involved in Ras-Raf, Ras-PI3K, and Ras-RalGDS interactions. Residues on the PPI interfaces are highlighted in red and hot-spot residues are underlined. Residues correspond to P4 are highlighted with red boxes.

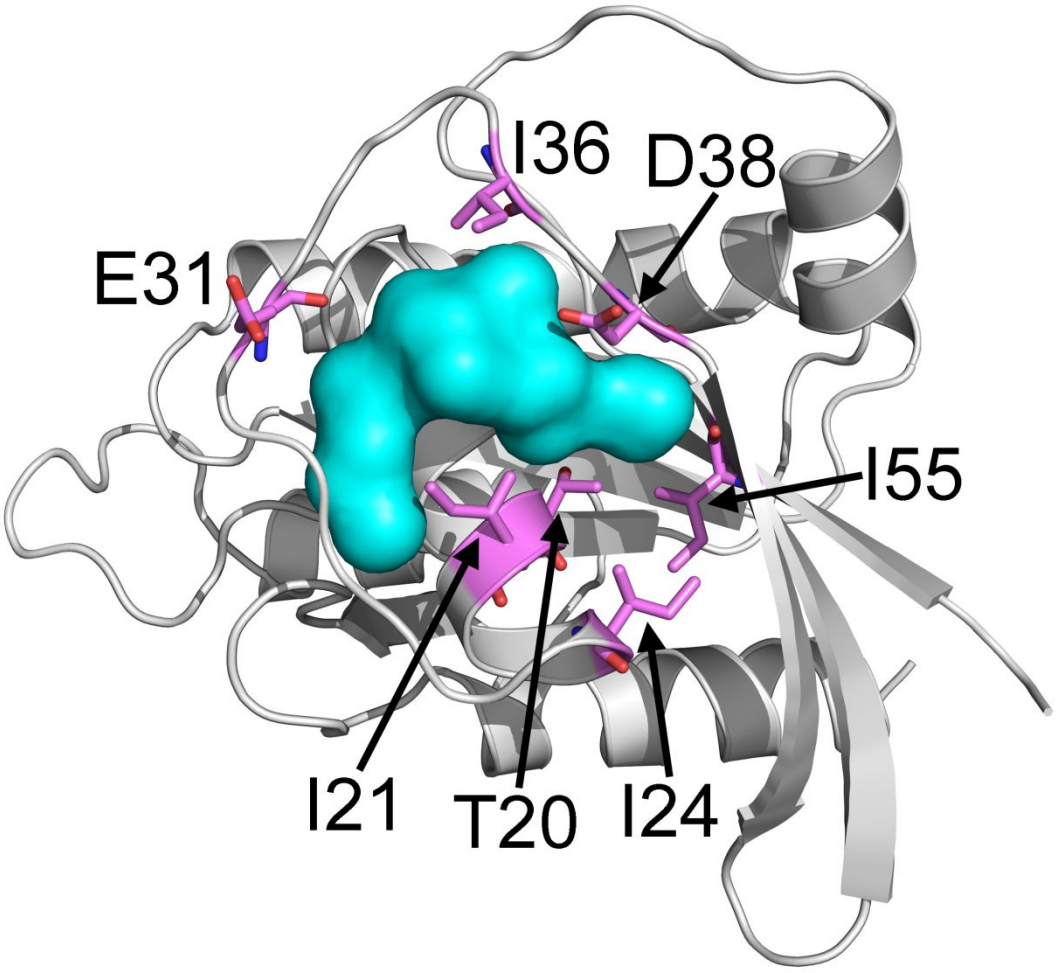

Figure S15. Structural overview of the critical residues within the predicted P4 pocket. Overall backbone of K-Ras is colored in gray, computational prediction probe is shown in cyan, and critical residues are displayed in pink.

Section 16: Protein Expression and Purification of K-Ras and GTP Hydrolysis Activity Assay

16.1 Protein Expression and Purification

The full-length human K-Ras4B cDNA was cloned into the pET42a bacterial expression plasmid using the NdeI and XhoI restriction sites, adding an N-terminal 6x histidine tag to ease protein purification as previously described.[105] Plasmid was transformed into *E.coli* Rosetta(DE3) cells for protein purification. The cells were induced with 0.5 mM isopropyl β-D-1-thiogalactopyranoside (IPTG) at 18℃. The protein was firstly purified with nickel column (GE healthcare) in the lysis buffer (50 mM HEPES, pH 7.4, 500 mM NaCl, 2 mM $MgCl_2$, and 20 mM imidazole), 1mM dithiothreitol and protein inhibitor cocktail was added before French Press. Then gel filtration chromatography was last purification step, using a Superdex 75 column (10/ 300 GL) with the following buffer (50 mM Tris-Citrate, pH 6.5, 50 mM NaCl, 5 mM $MgCl_2$, 0.01 mM Guanosine diphosphate and 1 mM dithiothreitol). Purification of mutation forms of K-Ras protein was carried out analogously.

16.2 GTP Hydrolysis Activity Assay

GTP hydrolysis activity was determined by measuring the release of inorganic phosphate from GTP using the EnzChek Phosphate Assay Kit (Invitrogen). The assay medium contained 50 mM Tris-HCl, 1 mM $MgCl_2$, pH 7.5, 0.2 mM 2-amino-6-mercapto-7-methylpurine ribonucleoside, 15 μM K-Ras4B protein, 1.0 units of purine nucleoside phosphorylase. The plate was incubated at room temperature for 10min. Then it was warmed to 37℃ in a microplate reader (BioTek, SYNERGY neo) and added 500 μM GTP to start the reaction. Absorbance was normalized to phosphate standards and initial rates were calculated. Each experiment was independently repeated three times in triplicate.

Section 17: Measurement of Enzymatic Activities by Ten Additional Mutations at the Periphery of the P4 Site

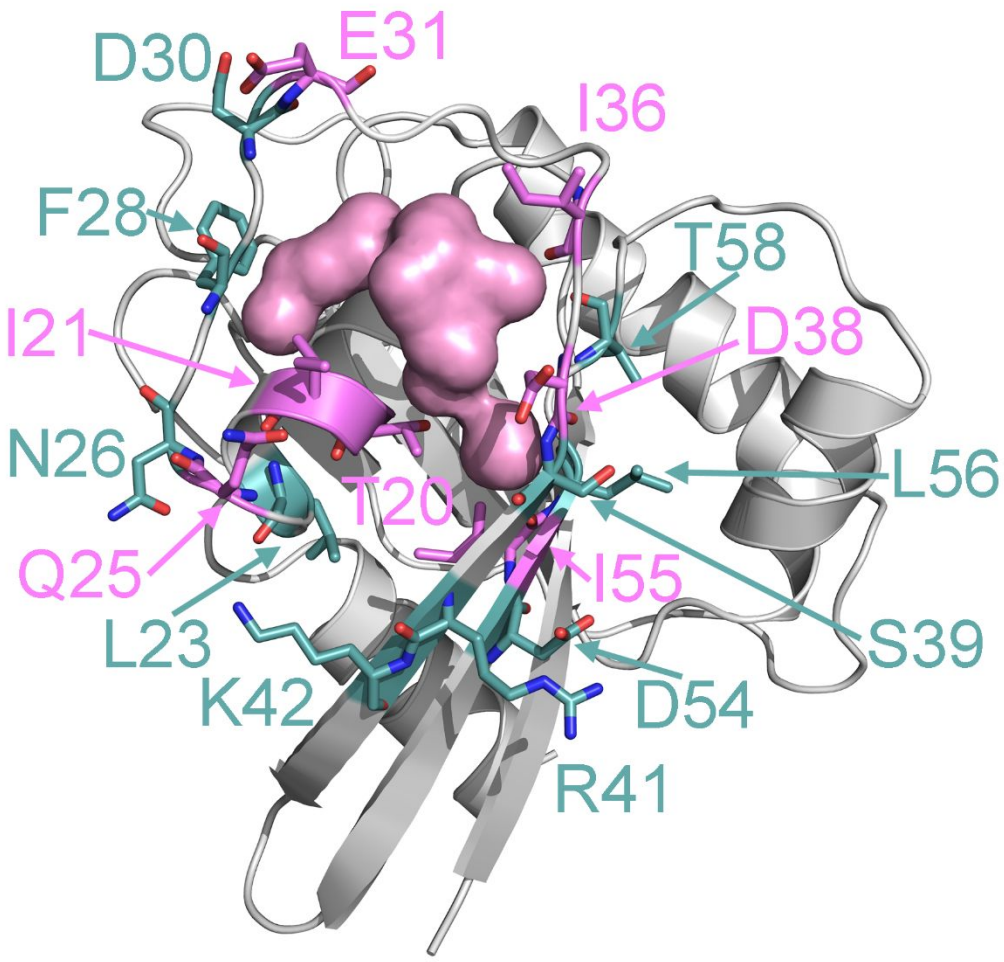

Figure S16: Structural overview of seven critical residues (T20, I21, Q25, E31, I36, D38, and I55) (colored in pink) within the predicted P4 site and ten residues (L23, N26, F28, D30, S39, R41, K42, D54, L56, and T58) (colored in light teal) at the periphery of the P4 site. Overall backbone of K-Ras is colored in gray and computational prediction probe of P4 site is shown in pink.

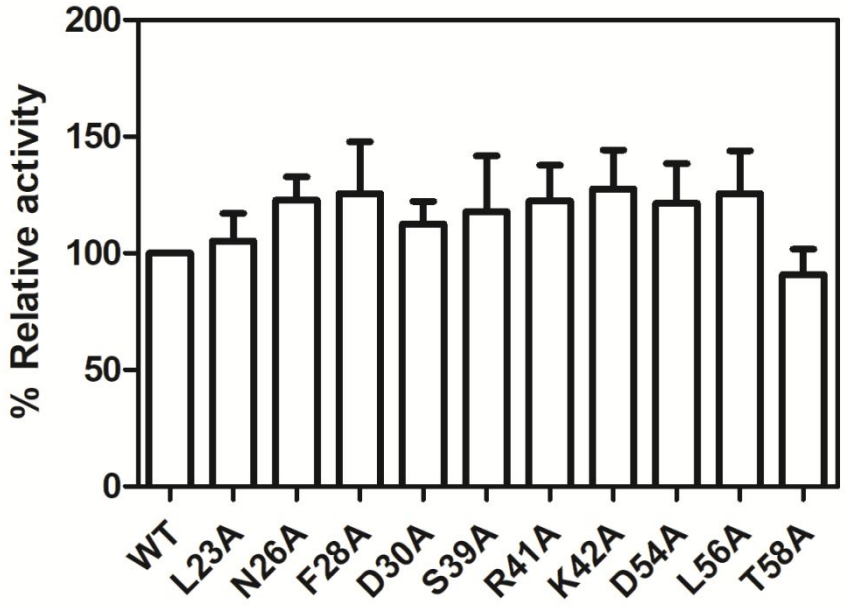

Figure S17: Mutagenesis experiments. The intrinsic GTP hydrolysis activity of ten Ras variants (L23A, N26A, F28A, D30A, S39A, R41A, K42A, D54A, L56A, and T58A) at the periphery of the P4 site was measured and the relative activities of each mutant are exhibited as a percentage of wild-type enzyme. The wild-type enzyme activity of Ras is represented as 100%. All assays were performed in triplicate, and the results are presented as average ± SD.

References

1. Ostrem, J. M.; Peters, U.; Sos, M. L.; Wells, J. A.; Shokat, K. M., K-Ras(G12C) Inhibitors Allosterically Control GTP Affinity and Effector Interactions. *Nature* **2013,** *503,*548-551.
2. Henkelman, G.; Jonsson, H., Improved Tangent Estimate in the Nudged Elastic Band Method for Finding Minimum Energy Paths and Saddle Points. *J. Chem. Phys.* **2000,** *113,*9978-9985.
3. Reblova, K.; Strelcova, Z.; Kulhanek, P.; Besseova, I.; Mathews, D. H.; Van Nostrand, K.; Yildirim, I.; Turner, D. H.; Sponer, J., An RNA Molecular Switch: Intrinsic Flexibility of 23S rRNA Helices 40 and 68 5'-UAA/5'-GAN Internal Loops Studied by Molecular Dynamics Methods. *J. Chem. Theory Comput.* **2010,** *6,*910-929.
4. Duan, Y.; Wu, C.; Chowdhury, S.; Lee, M. C.; Xiong, G.; Zhang, W.; Yang, R.; Cieplak, P.; Luo, R.; Lee, T.; Caldwell, J.; Wang, J.; Kollman, P., A Point-Charge Force Field for Molecular Mechanics Simulations of Proteins based on Condensed-Phase Quantum Mechanical Calculations. *J. Comput. Chem.* **2003,** *24,*1999-2012.
5. Wang, J.; Wolf, R. M.; Caldwell, J. W.; Kollman, P. A.; Case, D. A., Development and Testing of a General Amber Force Field. *J. Comput. Chem.* **2004,** *25,*1157-1174.
6. Bergonzo, C.; Campbell, A. J.; Walker, R. C.; Simmerling, C., A Partial Nudged Elastic Band Implementation for Use with Large or Explicitly Solvated Systems. *Int. J. Quantum Chem.* **2009,** *109,*3781.
7. Huang, M.; Lu, S.; Shi, T.; Zhao, Y.; Chen, Y.; Li, X.; Liu, X.; Huang, Z.; Zhang, J., Conformational Transition Pathway in the Activation Process of Allosteric Glucokinase. *PLoS One.* **2013,** *8,*e55857.
8. York, D. M.; Wlodawer, A.; Pedersen, L. G.; Darden, T. A., Atomic-Level Accuracy in Simulations of Large Protein Crystals. *Proc. Natl. Acad. Sci. U. S. A.* **1994,** *91,*8715-8718.
9. Markowitz, J.; Mal, T. K.; Yuan, C.; Courtney, N. B.; Patel, M.; Stiff, A. R.; Blachly, J.; Walker, C.; Eisfeld, A. K.; de la Chapelle, A.; Carson, W. E., 3rd. Structural Characterization of NRAS Isoform 5. *Protein Sci.* **2016,** *25,*1069-1074.
10. Johnson, C. W.; Reid, D.; Parker, J. A.; Salter, S.; Knihtila, R.; Kuzmic, P.; Mattos, C., The small GTPases K-Ras, N-Ras, and H-Ras have Distinct Biochemical Properties Determined by Allosteric Effects. *J. Biol. Chem.* **2017,** *292,*12981-12993.
11. Janes, M. R.; Zhang, J.; Li, L. S.; Hansen, R.; Peters, U.; Guo, X.; Chen, Y.; Babbar, A.; Firdaus, S. J.; Darjania, L.; Feng, J.; Chen, J. H.; Li, S.; Li, S.; Long, Y. O.; Thach, C.; Liu, Y.; Zarieh, A.; Ely, T.; Kucharski, J. M.; Kessler, L. V.; Wu, T.; Yu, K.; Wang, Y.; Yao, Y.; Deng, X.; Zarrinkar, P. P.; Brehmer, D.; Dhanak, D.; Lorenzi, M. V.; Hu-Lowe, D.; Patricelli, M. P.; Ren, P.; Liu, Y., Targeting KRAS Mutant Cancers with a Covalent G12C-Specific Inhibitor. *Cell* **2018,** *172,*578-589.
12. Nnadi, C. I.; Jenkins, M. L.; Gentile, D. R.; Bateman, L. A.; Zaidman, D.; Balius, T. E.; Nomura, D. K.; Burke, J. E.; Shokat, K. M.; London, N., Novel K-Ras G12C Switch-II Covalent Binders Destabilize Ras and Accelerate Nucleotide Exchange. *J. Chem. Inf. Model.* **2018,** *58,*464-471.

13. Lu, J.; Bera, A. K.; Gondi, S.; Westover, K. D., KRAS Switch Mutants D33E and A59G Crystallize in the State 1 Conformation. *Biochemistry* **2018,** *57,*324-333.
14. Parker, J. A.; Volmar, A. Y.; Pavlopoulos, S.; Mattos, C., K-Ras Populates Conformational States Differently from Its Isoform H-Ras and Oncogenic Mutant K-RasG12D. *Structure* **2018**, 26, 810-820.
15. McGee, J. H.; Shim, S. Y.; Lee, S. J.; Swanson, P. K.; Jiang, S. Y.; Durney, M. A.; Verdine, G. L., Exceptionally High-Affinity Ras Binders that Remodel its Effector Domain. *J. Biol. Chem.* **2018,** *293,*3265-3280.
16. Xu, S.; Long, B. N.; Boris, G. H.; Chen, A.; Ni, S.; Kennedy, M. A., Structural Insight into the Rearrangement of the Switch I Region in GTP-bound G12A K-Ras. *Acta. Crystallogr. D Struct. Biol.* **2017,** *73,*970-984.
17. Gentile, D. R.; Rathinaswamy, M. K.; Jenkins, M. L.; Moss, S. M.; Siempelkamp, B. D.; Renslo, A. R.; Burke, J. E.; Shokat, K. M., Ras Binder Induces a Modified Switch-II Pocket in GTP and GDP States. *Cell Chem. Biol.* **2017,** *24,*1455-1466 e1414.
18. Nussinov, R.; Wang, G.; Tsai, C. J.; Jang, H.; Lu, S.; Banerjee, A.; Zhang, J.; Gaponenko, V., Calmodulin and PI3K Signaling in KRAS Cancers. *Trends Cancer* **2017,** *3,*214-224.
19. Zeng, M.; Lu, J.; Li, L.; Feru, F.; Quan, C.; Gero, T. W.; Ficarro, S. B.; Xiong, Y.; Ambrogio, C.; Paranal, R. M.; Catalano, M.; Shao, J.; Wong, K. K.; Marto, J. A.; Fischer, E. S.; Janne, P. A.; Scott, D. A.; Westover, K. D.; Gray, N. S., Potent and Selective Covalent Quinazoline Inhibitors of KRAS G12C. *Cell Chem. Biol.* **2017,** *24,*1005-1016 e1003.
20. Kauke, M. J.; Traxlmayr, M. W.; Parker, J. A.; Kiefer, J. D.; Knihtila, R.; McGee, J.; Verdine, G.; Mattos, C.; Wittrup, K. D., An Engineered Protein Antagonist of K-Ras/B-Raf Interaction. *Sci. Rep.* **2017,** *7,*5831.
21. Guillard, S.; Kolasinska-Zwierz, P.; Debreczeni, J.; Breed, J.; Zhang, J.; Bery, N.; Marwood, R.; Tart, J.; Overman, R.; Stocki, P.; Mistry, B.; Phillips, C.; Rabbitts, T.; Jackson, R.; Minter, R., Structural and Functional Characterization of a DARPin which Inhibits Ras Nucleotide Exchange. *Nat. Commun.* **2017,** *8,*16111.
22. McGregor, L. M.; Jenkins, M. L.; Kerwin, C.; Burke, J. E.; Shokat, K. M., Expanding the Scope of Electrophiles Capable of Targeting K-Ras Oncogenes. *Biochemistry* **2017,** *56,*3178-3183.
23. Sogabe, S.; Kamada, Y.; Miwa, M.; Niida, A.; Sameshima, T.; Kamaura, M.; Yonemori, K.; Sasaki, S.; Sakamoto, J. I.; Sakamoto, K., Crystal Structure of a Human K-Ras G12D Mutant in Complex with GDP and the Cyclic Inhibitory Peptide KRpep-2d. *ACS Med. Chem. Lett.* **2017,** *8,*732-736.
24. Xiong, Y.; Lu, J.; Hunter, J.; Li, L.; Scott, D.; Choi, H. G.; Lim, S. M.; Manandhar, A.; Gondi, S.; Sim, T.; Westover, K. D.; Gray, N. S., Covalent Guanosine Mimetic Inhibitors of G12C KRAS. *ACS Med. Chem. Lett.* **2017,** *8,*61-66.
25. Welsch, M. E.; Kaplan, A.; Chambers, J. M.; Stokes, M. E.; Bos, P. H.; Zask, A.; Zhang, Y.; Sanchez-Martin, M.; Badgley, M. A.; Huang, C. S.; Tran, T. H.; Akkiraju, H.; Brown, L. M.; Nandakumar, R.; Cremers, S.; Yang, W. S.; Tong, L.; Olive, K. P.; Ferrando, A.; Stockwell, B. R., Multivalent Small-Molecule Pan-RAS Inhibitors. *Cell*

2017, *168,*878-889 e829.
26. Dharmaiah, S.; Bindu, L.; Tran, T. H.; Gillette, W. K.; Frank, P. H.; Ghirlando, R.; Nissley, D. V.; Esposito, D.; McCormick, F.; Stephen, A. G.; Simanshu, D. K., Structural Basis of Recognition of Farnesylated and Methylated KRAS4b by PDEdelta. *Proc. Natl. Acad. Sci. U. S. A.* **2016,** *113,*E6766-E6775.
27. Patricelli, M. P.; Janes, M. R.; Li, L. S.; Hansen, R.; Peters, U.; Kessler, L. V.; Chen, Y.; Kucharski, J. M.; Feng, J.; Ely, T.; Chen, J. H.; Firdaus, S. J.; Babbar, A.; Ren, P.; Liu, Y., Selective Inhibition of Oncogenic KRAS Output with Small Molecules Targeting the Inactive State. *Cancer Discov.* **2016,** *6,*316-329.
28. Hunter, J. C.; Manandhar, A.; Carrasco, M. A.; Gurbani, D.; Gondi, S.; Westover, K. D., Biochemical and Structural Analysis of Common Cancer-Associated KRAS Mutations. *Mol. Cancer Res.* **2015,** *13,*1325-1335.
29. Sun, Q.; Phan, J.; Friberg, A. R.; Camper, D. V.; Olejniczak, E. T.; Fesik, S. W., A Method for the Second-Site Screening of K-Ras in the Presence of a Covalently Attached First-Site Ligand. *J. Biomol. NMR* **2014,** *60,*11-14.
30. Hunter, J. C.; Gurbani, D.; Ficarro, S. B.; Carrasco, M. A.; Lim, S. M.; Choi, H. G.; Xie, T.; Marto, J. A.; Chen, Z.; Gray, N. S.; Westover, K. D., In situ Selectivity Profiling and Crystal Structure of SML-8-73-1, an Active Site Inhibitor of Oncogenic K-Ras G12C. *Proc. Natl. Acad. Sci. U. S. A.* **2014,** *111,*8895-8900.
31. Sun, Q.; Burke, J. P.; Phan, J.; Burns, M. C.; Olejniczak, E. T.; Waterson, A. G.; Lee, T.; Rossanese, O. W.; Fesik, S. W., Discovery of Small Molecules that Bind to K-Ras and Inhibit SOS-Mediated Activation. *Angew. Chem. Int. Ed. Engl.* **2012,** *51,*6140-6143.
32. Maurer, T.; Garrenton, L. S.; Oh, A.; Pitts, K.; Anderson, D. J.; Skelton, N. J.; Fauber, B. P.; Pan, B.; Malek, S.; Stokoe, D.; Ludlam, M. J.; Bowman, K. K.; Wu, J.; Giannetti, A. M.; Starovasnik, M. A.; Mellman, I.; Jackson, P. K.; Rudolph, J.; Wang, W.; Fang, G., Small-,olecule Ligands Bind to a Distinct Pocket in Ras and Inhibit SOS-Mediated Nucleotide Exchange Activity. *Proc. Natl. Acad. Sci. U. S. A.* **2012,** *109,*5299-5304.
33. Pai, E. F.; Krengel, U.; Petsko, G. A.; Goody, R. S.; Kabsch, W.; Wittinghofer, A., Refined Crystal Structure of the Triphosphate Conformation of H-ras P21 at 1.35 A Resolution: Implications for the Mechanism of GTP Hydrolysis. *EMBO J.* **1990,** *9,*2351-2359.
34. Tong, L. A.; de Vos, A. M.; Milburn, M. V.; Kim, S. H., Crystal Structures at 2.2 A Resolution of the Catalytic Domains of Normal Ras protein and an Oncogenic Mutant Complexed with GDP. *J. Mol. Biol.* **1991,** *217,*503-516.
35. Milburn, M. V.; Tong, L.; deVos, A. M.; Brunger, A.; Yamaizumi, Z.; Nishimura, S.; Kim, S. H., Molecular Switch for Signal Transduction: Structural Differences between Active and Inactive Forms of Protooncogenic Ras Proteins. *Science* **1990,** *247,*939-945.
36. Krengel, U.; Schlichting, I.; Scherer, A.; Schumann, R.; Frech, M.; John, J.; Kabsch, W.; Pai, E. F.; Wittinghofer, A., Three-Dimensional Structures of H-ras P21 Mutants: Molecular Basis for their Inability to Function as Signal Switch Molecules. *Cell* **1990,** *62,*539-548.

37. Franken, S. M.; Scheidig, A. J.; Krengel, U.; Rensland, H.; Lautwein, A.; Geyer, M.; Scheffzek, K.; Goody, R. S.; Kalbitzer, H. R.; Pai, E. F.; Wittinghofer, A. Three-Dimensional Structures and Properties of a Transforming and a Nontransforming Glycine-12 Mutant of $P21^{H\text{-}ras}$. *Biochemistry* **1993,** *32,*8411-8420.
38. Kraulis, P. J.; Domaille, P. J.; Campbell-Burk, S. L.; Van Aken, T.; Laue, E. D., Solution Structure and Dynamics of Ras P21.GDP Determined by Heteronuclear Three- and Four-Dimensional NMR Spectroscopy. *Biochemistry* **1994,** *33,*3515-3531.
39. Scheidig, A. J.; Sanchez-Llorente, A.; Lautwein, A.; Pai, E. F.; Corrie, J. E.; Reid, G. P.; Wittinghofer, A.; Goody, R. S., Crystallographic Studies on P21(H-ras) using the Synchrotron Laue method: Improvement of Crystal Quality and Monitoring of the GTPase Reaction at Different Time Points. *Acta. Crystallogr. D Biol. Crystallogr.* **1994,** *50,*512-520.
40. Scheidig, A. J.; Franken, S. M.; Corrie, J. E.; Reid, G. P.; Wittinghofer, A.; Pai, E. F.; Goody, R. S., X-ray Crystal Structure Analysis of the Catalytic Domain of the Oncogene Product P21H-Ras Complexed with Caged GTP and Mant dGppNHp. *J. Mol. Biol.* **1995,** *253,*132-150.
41. Schweins, T.; Scheffzek, K.; Assheuer, R.; Wittinghofer, A., The Role of the Metal Ion in the P21Ras Catalysed GTP-Hydrolysis: Mn2+ versus Mg2+. *J. Mol. Biol.* **1997,** *266,*847-856.
42. Ito, Y.; Yamasaki, K.; Iwahara, J.; Terada, T.; Kamiya, A.; Shirouzu, M.; Muto, Y.; Kawai, G.; Yokoyama, S.; Laue, E. D.; Walchli, M.; Shibata, T.; Nishimura, S.; Miyazawa, T., Regional Polysterism in the GTP-bound Form of the Human c-Ha-Ras Protein. *Biochemistry* **1997,** *36,*9109-9119.
43. Scheffzek, K.; Ahmadian, M. R.; Kabsch, W.; Wiesmuller, L.; Lautwein, A.; Schmitz, F.; Wittinghofer, A., The Ras-RasGAP Complex: Structural Basis for GTPase Activation and its Loss in Oncogenic Ras Mutants. *Science* **1997,** *277,*333-338.
44. Boriack-Sjodin, P. A.; Margarit, S. M.; Bar-Sagi, D.; Kuriyan, J., The Structural Basis of the Activation of Ras by SOS. *Nature* **1998,** *394,*337-343.
45. Dimopoulos, M. A.; Papadopoulou, M.; Andreopoulou, E.; Papadimitriou, C.; Pavlidis, N.; Aravantinos, G.; Aspropotamitis, A.; Anagnostopoulos, A.; Fountzilas, G.; Michalas, S.; Pectacides, D., Favorable Outcome of Ovarian Germ Cell Malignancies Treated with Cisplatin or Carboplatin-based Chemotherapy: A Hellenic Cooperative Oncology Group study. *Gynecol. Oncol.* **1998,** *70,*70-74.
46. Ahmadian, M. R.; Zor, T.; Vogt, D.; Kabsch, W.; Selinger, Z.; Wittinghofer, A.; Scheffzek, K., Guanosine Triphosphatase Stimulation of Oncogenic Ras Mutants. *Proc. Natl. Acad. Sci. U. S. A.* **1999,** *96,*7065-7070.
47. Scheidig, A. J.; Burmester, C.; Goody, R. S., The Pre-Hydrolysis State of P21(Ras) in Complex with GTP: New Insights into the Role of Water Molecules in the GTP Hydrolysis Reaction of Ras-like Proteins. *Structure* **1999,** *7,*1311-1324.
48. Pacold, M. E.; Suire, S.; Perisic, O.; Lara-Gonzalez, S.; Davis, C. T.; Walker, E. H.; Hawkins, P. T.; Stephens, L.; Eccleston, J. F.; Williams, R. L., Crystal Structure and Functional Analysis of Ras Binding to its Effector Phosphoinositide 3-Kinase Gamma. *Cell* **2000,** *103,*931-943.

49. Spoerner, M.; Herrmann, C.; Vetter, I. R.; Kalbitzer, H. R.; Wittinghofer, A., Dynamic Properties of the Ras Switch I Region and its Importance for Binding to Effectors. *Proc. Natl. Acad. Sci. U. S. A.* **2001,** *98,*4944-4949.
50. Kigawa, T.; Yamaguchi-Nunokawa, E.; Kodama, K.; Matsuda, T.; Yabuki, T.; Matsuda, N.; Ishitani, R.; Nureki, O.; Yokoyama, S., Selenomethionine Incorporation into a Protein by Cell-Free Synthesis. *J. Struct. Funct. Genomics* **2002,** *2,*29-35.
51. Scheffzek, K.; Grunewald, P.; Wohlgemuth, S.; Kabsch, W.; Tu, H.; Wigler, M.; Wittinghofer, A.; Herrmann, C., The Ras-Byr2RBD Complex: Structural Basis for Ras Effector Recognition in yeast. *Structure* **2001,** *9,*1043-1050.
52. Hall, B. E.; Bar-Sagi, D.; Nassar, N., The Structural Basis for the Transition from Ras-GTP to Ras-GDP. *Proc. Natl. Acad. Sci. U. S. A.* **2002,** *99,*12138-12142.
53. Margarit, S. M.; Sondermann, H.; Hall, B. E.; Nagar, B.; Hoelz, A.; Pirruccello, M.; Bar-Sagi, D.; Kuriyan, J., Structural Evidence for Feedback Activation by Ras.GTP of the Ras-specific Nucleotide Exchange Factor SOS. *Cell* **2003,** *112,*685-695.
54. Buhrman, G.; de Serrano, V.; Mattos, C., Organic Solvents Order the Dynamic Wwitch II in Ras Crystals. *Structure* **2003,** *11,*747-751.
55. Sondermann, H.; Soisson, S. M.; Boykevisch, S.; Yang, S. S.; Bar-Sagi, D.; Kuriyan, J., Structural Analysis of Autoinhibition in the Ras Activator Son of Sevenless. *Cell* **2004,** *119,*393-405.
56. Bunney, T. D.; Harris, R.; Gandarillas, N. L.; Josephs, M. B.; Roe, S. M.; Sorli, S. C.; Paterson, H. F.; Rodrigues-Lima, F.; Esposito, D.; Ponting, C. P.; Gierschik, P.; Pearl, L. H.; Driscoll, P. C.; Katan, M., Structural and Mechanistic Insights into Ras Association Domains of Phospholipase C epsilon. *Mol. Cell* **2006,** *21,*495-507.
57. Ford, B.; Hornak, V.; Kleinman, H.; Nassar, N., Structure of a Transient Intermediate for GTP Hydrolysis by Ras. *Structure* **2006,** *14,*427-436.
58. Klink, B. U.; Goody, R. S.; Scheidig, A. J., A Newly Designed Microspectrofluorometer for Kinetic Studies on Protein Crystals in Combination with X-ray Diffraction. *Biophys J.* **2006,** *91,*981-992.
59. Tanaka, T.; Williams, R. L.; Rabbitts, T. H., Tumour Prevention by a Single Antibody Domain Targeting the Interaction of Signal Transduction Proteins with RAS. *EMBO J.* **2007,** *26,*3250-3259.
60. Denayer, E.; Parret, A.; Chmara, M.; Schubbert, S.; Vogels, A.; Devriendt, K.; Frijns, J. P.; Rybin, V.; de Ravel, T. J.; Shannon, K.; Cools, J.; Scheffzek, K.; Legius, E., Mutation Analysis in Costello Syndrome: Functional and Structural Characterization of the HRAS p.Lys117Arg Mutation. *Hum. Mutat.* **2008,** *29,*232-239.
61. Buhrman, G.; Wink, G.; Mattos, C., Transformation Efficiency of RasQ61 Mutants Linked to Structural Features of the Switch Regions in the Presence of Raf. *Structure* **2007,** *15,*1618-1629.
62. Tanaka, T.; Rabbitts, T. H., Functional Intracellular Antibody Fragments do not Require Invariant intra-domain Disulfide Bonds. *J. Mol. Biol.* **2008,** *376,*749-757.
63. Stieglitz, B.; Bee, C.; Schwarz, D.; Yildiz, O.; Moshnikova, A.; Khokhlatchev, A.; Herrmann, C., Novel Type of Ras Effector Interaction Established between

Tumour Suppressor NORE1A and Ras Switch II. *EMBO J.* **2008,** *27,*1995-2005.
64. Cirstea, I. C.; Kutsche, K.; Dvorsky, R.; Gremer, L.; Carta, C.; Horn, D.; Roberts, A. E.; Lepri, F.; Merbitz-Zahradnik, T.; Konig, R.; Kratz, C. P.; Pantaleoni, F.; Dentici, M. L.; Joshi, V. A.; Kucherlapati, R. S.; Mazzanti, L.; Mundlos, S.; Patton, M. A.; Silengo, M. C.; Rossi, C.; Zampino, G.; Digilio, C.; Stuppia, L.; Seemanova, E.; Pennacchio, L. A.; Gelb, B. D.; Dallapiccola, B.; Wittinghofer, A.; Ahmadian, M. R.; Tartaglia, M.; Zenker, M., A Restricted Spectrum of NRAS Mutations causes Noonan Syndrome. *Nat. Genet.* **2010,** *42,*27-29.
65. Buhrman, G.; Holzapfel, G.; Fetics, S.; Mattos, C., Allosteric Modulation of Ras Positions Q61 for A Direct Role in Catalysis. *Proc. Natl. Acad. Sci. U. S. A.* **2010,** *107,*4931-4936.
66. Nassar, N.; Singh, K.; Garcia-Diaz, M., Structure of the Dominant Negative S17N Mutant of Ras. *Biochemistry* **2010,** *49,*1970-1974.
67. Filchtinski, D.; Sharabi, O.; Ruppel, A.; Vetter, I. R.; Herrmann, C.; Shifman, J. M., What makes Ras an Efficient Molecular Switch: A Computational, Biophysical, and Structural Study of Ras-GDP Interactions with Mutants of Raf. *J. Mol. Biol.* **2010,** *399,*422-435.
68. Shima, F.; Ijiri, Y.; Muraoka, S.; Liao, J.; Ye, M.; Araki, M.; Matsumoto, K.; Yamamoto, N.; Sugimoto, T.; Yoshikawa, Y.; Kumasaka, T.; Yamamoto, M.; Tamura, A.; Kataoka, T., Structural Basis for Conformational Dynamics of GTP-bound Ras Protein. *J. Biol. Chem.* **2010,** *285,*22696-22705.
69. Buhrman, G.; Kumar, V. S.; Cirit, M.; Haugh, J. M.; Mattos, C., Allosteric Modulation of Ras-GTP is Linked to Signal Transduction through RAF Kinase. *J. Biol. Chem.* **2011,** *286,*3323-3331.
70. Rosnizeck, I. C.; Graf, T.; Spoerner, M.; Trankle, J.; Filchtinski, D.; Herrmann, C.; Gremer, L.; Vetter, I. R.; Wittinghofer, A.; Konig, B.; Kalbitzer, H. R., Stabilizing a Weak Binding State for Effectors in the Human Ras Protein by Cyclen Complexes. *Angew. Chem. Int. Ed. Engl.* **2010,** *49,*3830-3833.
71. Buhrman, G.; O'Connor, C.; Zerbe, B.; Kearney, B. M.; Napoleon, R.; Kovrigina, E. A.; Vajda, S.; Kozakov, D.; Kovrigin, E. L.; Mattos, C., Analysis of Binding Site Hot spots on the Surface of Ras GTPase. *J. Mol. Biol.* **2011,** *413,*773-789.
72. Araki, M.; Shima, F.; Yoshikawa, Y.; Muraoka, S.; Ijiri, Y.; Nagahara, Y.; Shirono, T.; Kataoka, T.; Tamura, A., Solution Structure of the State 1 Conformer of GTP-bound H-Ras Protein and Distinct Dynamic Properties between the State 1 and State 2 Conformers. *J. Biol. Chem.* **2011,** *286,*39644-39653.
73. Fraser, J. S.; van den Bedem, H.; Samelson, A. J.; Lang, P. T.; Holton, J. M.; Echols, N.; Alber, T., Accessing Protein Conformational Ensembles using Room-Temperature X-ray Crystallography. *Proc. Natl. Acad. Sci. U. S. A.* **2011,** *108,*16247-16252.
74. Muraoka, S.; Shima, F.; Araki, M.; Inoue, T.; Yoshimoto, A.; Ijiri, Y.; Seki, N.; Tamura, A.; Kumasaka, T.; Yamamoto, M.; Kataoka, T., Crystal Structures of the State 1 Conformations of the GTP-bound H-Ras Protein and its Oncogenic G12V and Q61L Mutants. *FEBS Lett.* **2012,** *586,*1715-1718.
75. Holzapfel, G.; Buhrman, G.; Mattos, C., Shift in the Equilibrium between On and

Off States of the Allosteric Switch in Ras-GppNHp Affected by Small Molecules and Bulk Solvent Composition. *Biochemistry* **2012,** *51,*6114-6126.
76. Shima, F.; Yoshikawa, Y.; Ye, M.; Araki, M.; Matsumoto, S.; Liao, J.; Hu, L.; Sugimoto, T.; Ijiri, Y.; Takeda, A.; Nishiyama, Y.; Sato, C.; Muraoka, S.; Tamura, A.; Osoda, T.; Tsuda, K.; Miyakawa, T.; Fukunishi, H.; Shimada, J.; Kumasaka, T.; Yamamoto, M.; Kataoka, T., In silico Discovery of Small-Molecule Ras Inhibitors that Display Antitumor Activity by Blocking the Ras-Effector Interaction. *Proc. Natl. Acad. Sci. U. S. A.* **2013,** *110,*8182-8187.
77. Fetics, S. K.; Guterres, H.; Kearney, B. M.; Buhrman, G.; Ma, B.; Nussinov, R.; Mattos, C., Allosteric Effects of the Oncogenic RasQ61L Mutant on Raf-RBD. *Structure* **2015,** *23,*505-516.
78. Qamra, R.; Hubbard, S. R., Structural Basis for the Interaction of the Adaptor Protein Grb14 with Activated Ras. *PLoS One.* **2013,** *8,*e72473.
79. Burns, M. C.; Sun, Q.; Daniels, R. N.; Camper, D.; Kennedy, J. P.; Phan, J.; Olejniczak, E. T.; Lee, T.; Waterson, A. G.; Rossanese, O. W.; Fesik, S. W., Approach for Targeting Ras with Small Molecules that Activate SOS-mediated Nucleotide Exchange. *Proc. Natl. Acad. Sci. U. S. A.* **2014,** *111,*3401-3406.
80. Winter, J. J.; Anderson, M.; Blades, K.; Brassington, C.; Breeze, A. L.; Chresta, C.; Embrey, K.; Fairley, G.; Faulder, P.; Finlay, M. R.; Kettle, J. G.; Nowak, T.; Overman, R.; Patel, S. J.; Perkins, P.; Spadola, L.; Tart, J.; Tucker, J. A.; Wrigley, G., Small Molecule Binding Sites on the Ras:SOS Complex can be Exploited for Inhibition of Ras Activation. *J. Med. Chem.* **2015,** *58,*2265-2274.
81. Ting, P. Y.; Johnson, C. W.; Fang, C.; Cao, X.; Graeber, T. G.; Mattos, C.; Colicelli, J., Tyrosine Phosphorylation of RAS by ABL Allosterically Enhances Effector Binding. *FASEB J.* **2015,** *29,*3750-3761.
82. Tang, Y.; Huang, Y. J.; Hopf, T. A.; Sander, C.; Marks, D. S.; Montelione, G. T., Protein Structure Determination by Combining Sparse NMR Data with Evolutionary Couplings. *Nat. Methods.* **2015,** *12,*751-754.
83. Knihtila, R.; Holzapfel, G.; Weiss, K.; Meilleur, F.; Mattos, C., Neutron Crystal Structure of RAS GTPase Puts in Question the Protonation State of the GTP gamma-Phosphate. *J. Biol. Chem.* **2015,** *290,*31025-31036.
84. Matsumoto, S.; Miyano, N.; Baba, S.; Liao, J.; Kawamura, T.; Tsuda, C.; Takeda, A.; Yamamoto, M.; Kumasaka, T.; Kataoka, T.; Shima, F., Molecular Mechanism for Conformational Dynamics of Ras.GTP Elucidated from In-Situ Structural Transition in Crystal. *Sci. Rep.* **2016,** *6,*25931.
85. Spencer-Smith, R.; Koide, A.; Zhou, Y.; Eguchi, R. R.; Sha, F.; Gajwani, P.; Santana, D.; Gupta, A.; Jacobs, M.; Herrero-Garcia, E.; Cobbert, J.; Lavoie, H.; Smith, M.; Rajakulendran, T.; Dowdell, E.; Okur, M. N.; Dementieva, I.; Sicheri, F.; Therrien, M.; Hancock, J. F.; Ikura, M.; Koide, S.; O'Bryan, J. P., Inhibition of RAS Function through Targeting an Allosteric Regulatory Site. *Nat. Chem. Biol.* **2017,** *13,*62-68.
86. Bandaru, P.; Shah, N. H.; Bhattacharyya, M.; Barton, J. P.; Kondo, Y.; Cofsky, J. C.; Gee, C. L.; Chakraborty, A. K.; Kortemme, T.; Ranganathan, R.; Kuriyan, J., Deconstruction of the Ras Switching Cycle through Saturation Mutagenesis. *Elife.*

2017, *6*, e27810.
87. Ke, H.; Matsumoto, S.; Murashima, Y.; Taniguchi-Tamura, H.; Miyamoto, R.; Yoshikawa, Y.; Tsuda, C.; Kumasaka, T.; Mizohata, E.; Edamatsu, H.; Kataoka, T., Structural Basis for Intramolecular Interaction of post-translationally Modified H-Ras*GTP Prepared by Protein Ligation. *FEBS Lett.* **2017,** *591,*2470-2481.
88. Vercoulen, Y.; Kondo, Y.; Iwig, J. S.; Janssen, A. B.; White, K. A.; Amini, M.; Barber, D. L.; Kuriyan, J.; Roose, J. P., A Histidine pH Sensor Regulates Activation of the Ras-specific Guanine Nucleotide Exchange Factor RasGRP1. *Elife* **2017,** *6*, e29002.
89. Smith, M. J.; Ottoni, E.; Ishiyama, N.; Goudreault, M.; Haman, A.; Meyer, C.; Tucholska, M.; Gasmi-Seabrook, G.; Menezes, S.; Laister, R. C.; Minden, M. D.; Marschalek, R.; Gingras, A. C.; Hoang, T.; Ikura, M., Evolution of AF6-RAS Association and its Implications in Mixed-lineage Leukemia. *Nat. Commun.* **2017,** *8,*1099.
90. Harrigan, M. P.; Sultan, M. M.; Hernandez, C. X.; Husic, B. E.; Eastman, P.; Schwantes, C. R.; Beauchamp, K. A.; McGibbon, R. T.; Pande, V. S., MSMBuilder: Statistical Models for Biomolecular Dynamics. *Biophys J.* **2017,** *112,*10-15.
91. Beauchamp, K. A.; Bowman, G. R.; Lane, T. J.; Maibaum, L.; Haque, I. S.; Pande, V. S., MSMBuilder2: Modeling Conformational Dynamics at the Picosecond to Millisecond Scale. *J. Chem. Theory Comput.* **2011,** *7,*3412-3419.
92. Bowman, G. R., A Tutorial on Building Markov State Models with MSMBuilder and Coarse-Graining them with BACE. *Methods Mol. Biol.* **2014,** *1084,*141-158.
93. Perez-Hernandez, G.; Paul, F.; Giorgino, T.; De Fabritiis, G.; Noe, F., Identification of Slow Molecular Order Parameters for Markov Model Construction. *J. Chem. Phys.* **2013,** *139,*015102.
94. Scherer, M. K.; Trendelkamp-Schroer, B.; Paul, F.; Perez-Hernandez, G.; Hoffmann, M.; Plattner, N.; Wehmeyer, C.; Prinz, J. H.; Noe, F., PyEMMA 2: A Software Package for Estimation, Validation, and Analysis of Markov Models. *J. Chem. Theory Comput.* **2015,** *11,*5525-5542.
95. Singhal, N.; Pande, V. S., Error Analysis and Efficient Sampling in Markovian State Models for Molecular Dynamics. *J. Chem. Phys.* **2005,** *123,*204909.
96. Singhal, N.; Snow, C. D.; Pande, V. S., Using Path Sampling to Build Better Markovian State Models: Predicting the Folding Rate and Mechanism of a Tryptophan Zipper Beta Hairpin. *J. Chem. Phys.* **2004,** *121,*415-425.
97. Wittinghofer, A.; Scheffzek, K.; Ahmadian, M. R., The Interaction of Ras with GTPase-activating Proteins. *FEBS Lett.* **1997,** *410,*63-67.
98. Shutes, A.; Der, C. J., Real-time in vitro Measurement of Intrinsic and Ras GAP-mediated GTP Hydrolysis. *Methods Enzymol.* **2006,** *407,*9-22.
99. Shukla, D.; Meng, Y.; Roux, B.; Pande, V. S., Activation Pathway of Src Kinase Reveals Intermediate States as Targets for Drug Design. *Nat. Commun.* **2014,** *5,*3397.
100. Schmidtke, P.; Le Guilloux, V.; Maupetit, J.; Tuffery, P., Fpocket: Online Tools for Protein Ensemble Pocket Detection and Tracking. *Nucleic Acids. Res.* **2010,** *38,*W582-589.
101. Le Guilloux, V.; Schmidtke, P.; Tuffery, P., Fpocket: An Open Source Platform

for Ligand Pocket Detection. *BMC Bioinformatics* **2009,** *10,*168.
102. Gao, M.; Skolnick, J., APoc: Large-scale Identification of Similar Protein Pockets. *Bioinformatics* **2013,** *29,*597-604.
103. Krissinel, E.; Henrick, K., Inference of Macromolecular Assemblies from Crystalline State. *J. Mol. Biol.* **2007,** *372,*774-797.
104. Huang, L.; Hofer, F.; Martin, G. S.; Kim, S. H., Structural Basis for the Interaction of Ras with RalGDS. *Nat. Struct. Biol.* **1998,** *5,*422-426.
105. Abraham, S. J.; Muhamed, I.; Nolet, R.; Yeung, F.; Gaponenko, V., Expression, Purification, and Characterization of Soluble K-Ras4B for Structural Analysis. *Protein Expr. Purif.* **2010,** *73,*125-131.